International Journal of Plasticity 183 (2024) 104153

Contents lists available at ScienceDirect

International Journal of Plasticity

journal homepage: www.elsevier.com/locate/ijplas

Fast Fourier transform approach to Strain Gradient Crystal Plasticity: Regularization of strain localization and size effect

Amirhossein Lame Jouybari [a,b,*], Samir El Shawish [a], Leon Cizelj [a,b]

[a] Jožef Stefan Institute, Jamova cesta 39, Ljubljana, Sl-1000, Slovenia
[b] University of Ljubljana, Jadranska ulica 19, Ljubljana, Sl-1000, Slovenia

ARTICLE INFO

Keywords:
Strain localization A
Strain gradient crystal plasticity B
Polycrystalline material B
FFT-homogenization method C
Regularization C

ABSTRACT

The Strain Gradient Crystal Plasticity (SGCP) model, based on cumulative shear strain, is developed to regularize and simulate the size effect behavior of polycrystalline aggregates, specifically addressing the formation of localization bands, such as slip and kink bands, influenced by strain softening during the initial stages of plastic deformation. In this respect, the thermodynamically consistent derivation of the SGCP equations is presented, establishing their connection to the kinematics of classical crystal plasticity (CCP) framework. The governing balance equations are solved using the fixed-point algorithm of the fast Fourier transform (FFT)-homogenization method, involving explicit coupling between the classical and SGCP balance equations. To address this problem, a strong 21-voxel finite difference scheme is established. This scheme is considered to solve the higher order balance equation inherent to SGCP. Additionally, three types of interface conditions are implemented to explore the impact of grain boundaries on the transmission of localization bands. These conditions yield consistent intragranular/transgranular localization patterns in the MicroFree and MicroContinuity cases, while in the MicroHard condition all localization bands are intragranular with stress concentrations appearing at the grain boundaries.

Analytical solutions corresponding to different material behaviors are developed and compared with numerical results to validate the numerical implementation of the FFT fixed-point algorithm. It is observed that both the macroscopic behavior and microscopic variables in CCP framework are highly influenced by grid resolutions (non-objective), leading to numerical instabilities arising from the material softening and subsequent formation of localization bands, both in single crystals and polycrystalline aggregates. Remarkably, the developed SGCP model provides results that are independent of grid resolutions (objective) and effectively regularizes the material behavior on local scale. Moreover, the non-local parameter of the model is capable of controlling the localization band widths. Finally, the proposed SGCP model, together with employed MicroHard condition on grain boundaries, is demonstrated to qualitatively reproduce main microstructural features of irradiated polycrystalline materials.

1. Introduction

The study of heterogeneity in dislocation glide during plastic deformation of crystals has been a long-established focus in solid mechanics, aiming to generate a connection between microscopic and macroscopic behaviors. As a consequence of this heterogeneity, strain localization has been observed, manifesting as necking, buckling, shear bands, Lüders bands, etc. Generally, this phenomenon

* Corresponding author at: Jožef Stefan Institute, Jamova cesta 39, Ljubljana, Sl-1000, Slovenia.
E-mail address: Amirhossein.Lame@ijs.si (A. Lame Jouybari).

https://doi.org/10.1016/j.ijplas.2024.104153
Received 14 March 2024; Received in revised form 17 October 2024
Available online 29 October 2024

results from mechanical instability, which can be divided into global and material types. For instance, necking and buckling stem from global instability (Hart, 1967), while shear bands are associated with material instability (Rice, 1976). From a computational perspective, global instability arises from the loss of solution uniqueness or the null determinant of the tangent operator (singularity). Conversely, material instability occurs in cases of strain softening behavior, resulting in a discontinuity in strain rate within the interface of the shear bands. Depending on the coupling of thermal effects and plastic deformation, shear bands are typically characterized into isothermal or adiabatic types (Zener and Hollomon, 1944; Rogers, 1979). Pioneering work (Asaro and Rice, 1977) conducted a bifurcation analysis, categorizing two potential (isothermal) bands with different orientations in single crystals: slip bands (parallel to the slip plane) and kink bands (perpendicular to the slip direction). Moreover, a particular utilization of these bands is microscopically evident in irradiated solids. In such solids, hardening defects like Frank dislocation loops are introduced within the material as a result of irradiation (Cui and Po, 2018). When dislocations start to glide within the material, they eliminate these defects, leading to the formation of localized softened paths (Mahajan and Eyre, 2017). This phenomenon is commonly referred to as clear channel or dislocation channeling mechanism. This mechanism has a significant impact on the macroscopic mechanical properties of materials used in nuclear power plants, such as austenitic stainless steels and Zircaloys. For example, loss of toughness and ductility, increasing of yield stress and reduction of work hardening domain have been experimentally observed in irradiated austenitic stainless steels (Pokor et al., 2004). Furthermore, dislocations can interact with grain boundaries in corrosive environments like nuclear reactor and contribute to the mechanism of Irradiation Assisted Stress Corrosion Cracking (IASCC) (McMurtrey et al., 2011), or interact with other radiation-induced defects such as voids or bubbles (Scherer et al., 2019).

Conventional theories, in particular the classical crystal plasticity (CCP) finite element method (Erinosho and Dunne, 2015; El Shawish et al., 2020; Hure et al., 2016; El Shawish and Cizelj, 2017; Lame Jouybari et al., 2023; Hardie et al., 2023), have been employed in the numerical simulations of irradiated and unirradiated solids. However, these theories cannot predict size effect behavior and often lead to ill-posed problems during (strain) localization process which is theoretically characterized by a shift in the form of the governing differential equations from hyperbolic to elliptic or contrariwise (Needleman, 1988). Hence, the results obtained from these classical theories frequently depend on the chosen discretization techniques and size of elements which is a consequence of the loss of ellipticity and stability (Lorentz and Benallal, 2005). For instance, the width of the localization bands is typically equivalent to one element width; accordingly, when the discretization becomes finer, the width becomes smaller. The literature presents two main strategies to overcome this numerical issue. One approach is to consider the element size as a material parameter that can be determined through experimental testing. This approach, however, introduces additional costs and relies on prior knowledge of where within the microstructure localization is probable to occur (Achouri et al., 2013; Xue et al., 2010). An alternative solution is to integrate non-local theory into the conventional methods. This theory postulates that the behavior of each material point is influenced not only by its own state but also by that of the finite number of its surrounding neighbors, and the width of the localization region is controlled by considering the gradient of the appropriate internal variable and material length scale (non-local parameter). Initially, such a material length scale was incorporated into the conventional crystal plasticity framework by adding the plastic strain gradient within the yield function to address the width of localization bands (Aifantis, 1984, 1987) and to eliminate strain singularities in front of the crack tip (Aifantis, 1992). Later, the framework has been updated to account for large deformations (Gurtin, 2008; Clayton et al., 2004; Clayton, 2010). Also, different length scales have been proposed in the framework of viscous strain gradient crystal plasticity theory based on the energetic and dissipative gradient of shear strain associated to each slip system and in application to the voided crystals by Niordson and Kysar (2014) which is followed to incremental flow theory by Nellemann et al. (2017). The non-local theory has been successfully applied in various domains to regularize the material behaviors, including the study of void growth and coalescence (Ling et al., 2018), in analyzing ductile fracture through a non-local relationship among dislocation density, plastic deformation, areas of defectiveness, damage regularization (Boeff et al., 2014; Al-Rub et al., 2015; Scherer et al., 2019; Tang et al., 2023; Lindroos et al., 2022), and grain boundaries (Zhang et al., 2023). The presence of grain boundaries poses a significant obstacle for slip/twin transfer, necessitating a specialized treatment in computational analyses of polycrystalline aggregates (Kameda and Zikry, 1998; Rezvanian et al., 2007; Ahmadikia et al., 2021, 2023; You et al., 2023).

Experimental testing on metallic alloys has revealed the size effect behavior, commonly referred to as the Hall-Petch effect, through tensile tests on mild steels (Hall, 1951; Petch, 1953) and torsion tests on thin wires (Fleck and Hutchinson, 1997). To incorporate this effect into crystal plasticity theory, the concepts of Statistically Stored Dislocation (SSD) and Geometrically Necessary Dislocation (GND) have been introduced, which have led to the development of strain gradient plasticity theory. The SSD density typically increases with plastic deformation and is associated with dislocations that glide through the microstructure and trap other dislocations. In contrast, GND is related to variations in plastic flow (attributable to the strain gradient). It is widely accepted that SSDs contribute to material hardening, akin to increasing the strength of the crystal (or the critical resolved shear stress), while GNDs contribute to additional hardening due to the size effect. The GND density in the microstructure is typically evaluated using Nye's tensor (Nye, 1953). However, based on the decomposition of edge and screw dislocations, the GND density can also be calculated using the gradient of shear strain (Arsenlis and Parks, 1999). Consequently, strain gradient crystal plasticity that accounts for the size effect and considers GNDs has been developed based on Nye's tensor (Gurtin, 2002; Cermelli and Gurtin, 2002), and micromorphic crystal plasticity has been formulated based on the gradient of shear strain (Wulfinghoff and Böhlke, 2012) to capture GNDs.

Within the field of solid mechanics, the regularization of governing constitutive equations is employed to smooth discontinuous variables such as plastic strain (Forest, 2016). Specifically, this method has been incorporated into the treatment of material softening and size effect behaviors (Peerlings et al., 2012) to achieve discretization-independent (objective) numerical results, which involve the Laplacian operator within the Helmholtz differential equation. Typically, this equation is regarded as a higher order balance equation, and its coupling with classical constitutive equations is ensured through a thermodynamic formulation involving higher

order stresses and traction tensors (Forest, 2009). Various types of regularization methods are discussed in the literature, including formulations that utilize additional degrees of freedom (Forest, 2009) and gradient terms (Waffenschmidt et al., 2014). In particular, the micromorphic crystal plasticity theory has been developed to account for the gradient of micromorphic variable as an additional degree of freedom which is interpreted as a counterpart of a single scalar total cumulative shear strain variable, as demonstrated in the works of Wulfinghoff et al. (2013), Ling et al. (2018), Scherer et al. (2019). This approach is termed as the MicroSlip micromorphic crystal plasticity model. In this development, to ensure the equality between the micromorphic variable and total cumulative shear strain, a substantial penalty modulus is introduced alongside the non-local parameter, which provides two effective parameters. In this way, the micromorphic crystal plasticity model can be seen as a relaxed (i.e., not strict) strain gradient plasticity model. In addition, in Scherer et al. (2020), a Lagrange multiplier based approach has been proposed as another way of deriving a relaxed strain gradient formulation.

The inception of the first FFT-homogenization method dates back to 1998 within the context of mechanical behavior of heterogeneous materials (Moulinec and Suquet, 1998) which is relatively recent in comparison to the Finite Element Method (FEM). The remarkable progress of the FFT-homogenization method in CCP framework (Lebensohn et al., 2012; Eisenlohr et al., 2013; Marano et al., 2019; Lucarini and Segurado, 2019; Dadhich and Alankar, 2022; Eghtesad et al., 2022) has recently extended to damage mechanics in large deformation (Cocke et al., 2023), elastic micropolar composites (Francis et al., 2024), strain localization in nano-metallic laminates by the irregular grid in the initial configuration (Zecevic et al., 2022), interface-dominated plasticity of nano-metallic laminates (Zecevic et al., 2023), size effects and reversible plasticity (Berbenni et al., 2020), cohesive composite voxels for fracture of materials (Chen et al., 2021). Furthermore, the method has been developed toward SGCP (Lebensohn and Needleman, 2016) by explicit coupling between classical and strain gradient governing equations using same strategy as the Nye's tensor-based field dislocation mechanics formulation (Berbenni et al., 2014; Brenner et al., 2014). These studies computationally solved the higher order balance equation from SGCP by transferring the equation into Fourier space, allowing for precise and fast computation of differentiation operators (like divergence, curl, gradient, etc.) of internal variables using special properties of the Fourier transform.

In the context of irradiated structural materials, a recent study by Marano et al. (2021) investigated the capability of MicroCurl SGCP model based on the curl of the plastic part of displacement gradient tensor as a strain gradient variable to predict the emergence and stability of intragranular localization (shear) bands in polycrystalline aggregates. The study employed a phenomenological exponential softening law to trigger the formation of these bands under applied macroscopic loading. Utilizing the SGCP approach, which incorporates the energy stored by geometrically necessary dislocations (linked to the lattice curvature) by the curl of the plastic part of displacement gradient tensor as the strain gradient variable along with two non-local parameters in terms of the average grain size and critical resolved shear stress, the research was performed using a highly parallel FFT-based solver within polycrystalline aggregates. The results demonstrated that the model breaks the equivalence between slip and kink bands, showing the replacement of the thick kink bands by the bundle of slip bands intragranularly within the crystals. This leads to a more accurate simulation of plastic slip fields in materials prone to intense slip localization. However, the model provides non-regularized spacings and a non-regularized number of slip bands, which makes the results grid dependent (non-objective). Unstable results were obtained also in single crystal simulations with material softening behavior. This indicates that further refinement of the SGCP model or its alternative may be required. Additionally, the study (Marano et al., 2021) addressed various implementations of higher order interface conditions based on the higher order traction tensor in terms of the curl of plastic part of displacement gradient tensor, to investigate the potential effect of grain boundaries on plastic deformation transmission between neighboring grains, as recently reported (Zhang et al., 2022). It was found that these interface conditions mainly influence the intensity of the localization (shear) bands without altering the pattern formation. Therefore, the exploration of alternative SGCP models, which could impact the localization pattern and potentially regulate the distribution of slip and kink bands, remains to be explored.

The primary goal of this study is to address the issue of localization (shear) band instability observed in single crystal and polycrystalline aggregates of irradiated structural materials under mechanical loading, and to thoroughly examine different higher order interface conditions at grain boundaries relevant for slip transfer. To achieve this, new (strict) MicroSlip SGCP model based on cumulative shear strain associated with each slip system is developed and proposed. Moreover, the impact of grain boundaries on slip transmission is elucidated by introducing new higher order traction stress and imposing various conditions on grain boundaries. The model is formulated within a thermodynamically consistent framework and implemented into an in-house code (Matlab, 2022) using newly upgraded fixed-point algorithm of the FFT-homogenization method. Here, several computational modifications to the fixed-point algorithm are incorporated with respect to the original version, to improve numerical accuracy and reduce oscillations in areas of the microstructure with high variations in material properties due to localization and higher order interface conditions. Once the MicroSlip SGCP framework is developed and FFT fixed-point algorithm upgraded, analytical closed-form solutions are derived from the SGCP theory in the case of a single slip associated with linear hardening, perfect plasticity, and linear softening behaviors. After validating the FFT implementation against these analytical solutions, the FFT-based solver is used to investigate the evolution and stability of localization (isothermal shear) bands in irradiated-like polycrystalline materials. This includes a focused examination of the critical role of grain boundaries which affect the transmission of the bands and their subsequent impact on local stress concentrations. For this purpose, a 2D plane strain periodic aggregate unit cell, comprising 200 randomly oriented columnar grains each with one active slip system, is considered and subjected to tensile loading. A recently proposed exponential softening behavior for plastic flow is used in order to trigger the localization and model the softening due to clearing of irradiation defects by the dislocation channeling mechanism. In addition, the microstructure size effect and impact of a single intrinsic length scale (non-local parameter) of the SGCP model are investigated. This is aimed at controlling the transmission of localization bands through grain boundaries and regularizing both slip and kink bands.

The paper is outlined as follows. Section 2.1 presents a thermodynamically consistent derivation of the SGCP (MicroSlip) constitutive equations within the context of the localization problem. Section 2.2 provides the FFT-homogenization method and the implementation of the fixed point algorithm used in this study. In Section 3.1, the analytical solutions for the SGCP model corresponding to different material behaviors are established. Section 3 encompasses the results of the single crystal and polycrystalline aggregate, including a comparison of numerical results with analytical solutions, the regularization of localization bands in single crystals and polycrystals, and an exploration of the role of grain boundaries and microstructure size effects on the evolution of localization patterns. Finally, a comparison with existing experimental results is performed and discussed.

The notation used in this study includes scalar, first-order (vector), second-order, and fourth-order tensors represented as X, $\underline{X}$, $\underline{\underline{X}}$, and $\underline{\underline{\underline{\underline{X}}}}$, respectively. Superscripts $^{\mathrm{tot}}$, $^{\mathrm{e}}$, $^{\mathrm{p}}$, $\dot{\cdot}$, $\hat{\cdot}$, *, and $\bar{\cdot}$ are utilized to signify the total, elastic, plastic, time derivative, Fourier transform, fluctuation, and spatial mean value part of the variable, respectively. Additionally, mathematical symbols such as $\otimes$, $*$, $.$, $:$, ∇, and Δ denote the tensor product, convolution, dot product, double contraction, gradient, and Laplacian operators. The Cartesian coordinate basis is denoted as $(\underline{e}_1, \underline{e}_2, \underline{e}_3)$, and the Einstein's summation convention is used in indicial representations.

2. Material and methods

This section introduces the proposed strict MicroSlip SGCP model and the improved FFT-homogenization method that are developed in this study.

2.1. MicroSlip strain gradient crystal plasticity model

In the framework of infinitesimal strain, a crystal lattice is assumed with N_α slip systems, slip directions and normals to slip planes $(\underline{s}^\alpha, \underline{m}^\alpha)$. In this framework, the total displacement gradient tensor undergoes additive decomposition into its elastic and plastic parts, Eq. (1). The elastic strain is identified as the symmetric part of the elastic displacement gradient tensor, Eq. (2), and the rate of plastic displacement tensor is defined by the process of dislocation glide in all active slip systems, Eq. (3).[1]

$$(\nabla \underline{u})^{\mathrm{tot}} = (\nabla \underline{u})^{\mathrm{e}} + (\nabla \underline{u})^{\mathrm{p}} \tag{1}$$

$$\underline{\underline{\varepsilon}}^{\mathrm{e}} = \frac{1}{2}\left((\nabla \underline{u})^{\mathrm{e}} + (\nabla \underline{u})^{\mathrm{eT}}\right) \tag{2}$$

$$(\dot{\nabla} \underline{u})^{\mathrm{p}} = \sum_{\alpha}^{N_\alpha} \dot{\gamma}^\alpha \underline{s}^\alpha \otimes \underline{m}^\alpha \tag{3}$$

The total cumulative shear strain is a history-dependent scalar variable, which is positive definite and increases due to plastic deformation and is defined by Eq. (4), following previous studies in the reduced micromorphic crystal plasticity model (Wulfinghoff et al., 2013; Ling et al., 2018). Inspired from these studies, the cumulative shear strain associated with slip system, Eq. (5), is chosen as a thermodynamic internal variable to incorporate strain gradient effect.

$$\gamma^{\mathrm{tot}}_{cum} = \int_0^{\mathrm{t}} \sum_{\alpha}^{N_\alpha} \left|\dot{\gamma}^\alpha\right| d\mathrm{t} \tag{4}$$

$$\gamma^{\alpha}_{cum} = \int_0^{\mathrm{t}} \left|\dot{\gamma}^\alpha\right| d\mathrm{t} \tag{5}$$

In the context of static deformation and the absence of body and inertial forces, the principle of virtual power is formulated for any subdomain of the body ($B \subseteq \mathcal{B}$) and its boundary ($\partial B \subseteq \partial \mathcal{B}$) in terms of the internal and contact power densities.

$$\int_B \left(\underline{\underline{\sigma}} : (\dot{\nabla} \underline{u})^{\mathrm{tot}} + \sum_\alpha^{N_\alpha} S^\alpha \dot{\gamma}^\alpha_{\mathrm{cum}} + \sum_\alpha^{N_\alpha} \underline{M}^\alpha . \underline{\dot{Q}}^\alpha\right) dV = \int_{\partial B} \left(\underline{t} . \dot{\underline{u}}^{\mathrm{tot}} + \sum_\alpha^{N_\alpha} m^\alpha \dot{\gamma}^\alpha_{\mathrm{cum}}\right) dS \qquad \forall \dot{\underline{u}}^{\mathrm{tot}},\ \forall \dot{\gamma}^\alpha_{\mathrm{cum}},\ \forall B \subseteq \mathcal{B},\ \forall \partial B \subseteq \partial \mathcal{B} \tag{6}$$

where σ represents the Cauchy stress tensor, S^α and $\underline{M}^\alpha$ are higher order stress tensors associated with strain gradient effects, $\underline{Q}^\alpha = \tilde{\nabla} \gamma^\alpha_{\mathrm{cum}}$ represents the higher order thermodynamic variable, and $\underline{t}$ stands for the classical Cauchy traction vector, while m^α signifies higher order scalar traction. As a consequence, for each material point within the crystal $\mathcal{B}$, both the Cauchy stress tensor and higher order stress tensors satisfy the following pair of balance equations during deformation in terms of the classical linear momentum balance equation, Eq. (7), and higher order balance equation, Eq. (8).

$$\nabla . \underline{\underline{\sigma}} = \underline{0} \quad \forall \underline{x} \in \mathcal{B} \tag{7}$$

$$\nabla . \underline{M}^\alpha - S^\alpha = 0 \quad \forall \underline{x} \in \mathcal{B},\ \forall \alpha \in N_\alpha \tag{8}$$

Additionally, at each material point on the boundary of the crystal, the stress tensors are observed to be in a state of equilibrium with the classical traction vector and scalar traction, serving as the prescribed boundary conditions.

$$\underline{t} = \underline{\underline{\sigma}} . \underline{n} \quad \forall \underline{x} \in \partial \mathcal{B} \tag{9}$$

$$m^\alpha = \underline{M}^\alpha . \underline{n} \quad \forall \underline{x} \in \partial \mathcal{B},\ \forall \alpha \in N_\alpha \tag{10}$$

[1] To avoid any misleading in notation the $(\dot{\nabla} \underline{u})^{\mathrm{p}} = (\frac{d}{dt}(\nabla \underline{u}))^{\mathrm{p}}$.

Here, $\underline{n}$ represents a unit vector denoting the outward surface normal. In the context of thermodynamics, the specific isothermal free energy potential is postulated to take on a straightforward quadratic form, reflective of the non-dissipative and dissipative energies during the deformation.

$$\psi = \psi(\underset{\sim}{\varepsilon}^{\mathrm{e}}, \gamma^{\alpha}_{\mathrm{cum}}, \nabla\gamma^{\alpha}_{\mathrm{cum}}) = \frac{1}{2\rho}\underset{\sim}{\varepsilon}^{\mathrm{e}} : \underset{\approx}{C} : \underset{\sim}{\varepsilon}^{\mathrm{e}} + \psi^{h}(\gamma^{\alpha}_{\mathrm{cum}}) + \sum_{\alpha}^{N_{\alpha}} \frac{1}{2\rho} A\underline{Q}^{\alpha}.\underline{Q}^{\alpha} \tag{11}$$

In this potential, the hyperelastic material is assumed for the elastic part of deformation, a strictly positive non-local parameter denoted as A serves to weight the gradient of the cumulative shear strain associated with each slip system,[2] $\psi^{h}(\gamma^{\alpha}_{cum})$ is the hardening potential, and ρ denotes the density of the crystal. From both the first and second principles of thermodynamics, the Clausius-Duhem inequality, under isothermal deformation conditions, implies that the internal power density (p_i stands for the left side of Eq. (6)) of the crystal is consistently greater than or equal to the free energy rate across the entire volume of the crystal.

$$p_i - \rho\dot{\psi} \geq 0 \tag{12}$$

Therefore, using chain rule in evaluating the time derivative of the free energy, the Clausius-Duhem inequality turns to the following equation.

$$\left(\underset{\sim}{\sigma} - \rho\frac{\partial\psi}{\partial\underset{\sim}{\varepsilon}^{\mathrm{e}}}\right) : \dot{\underset{\sim}{\varepsilon}}^{\mathrm{e}} + \underset{\sim}{\sigma} : (\nabla\underline{\dot{u}})^{\mathrm{p}} + \sum_{\alpha}^{N_{\alpha}}\left(S^{\alpha} - \rho\frac{\partial\psi^{h}}{\partial\gamma^{\alpha}_{\mathrm{cum}}}\right)\dot{\gamma}^{\alpha}_{\mathrm{cum}} + \sum_{\alpha}^{N_{\alpha}}\left(\underline{M}^{\alpha} - A\nabla\gamma^{\alpha}_{\mathrm{cum}}\right).\dot{\underline{Q}}^{\alpha} \geq 0 \tag{13}$$

Assumptions are made that both the power associated with the elastic part of the deformation and the gradient of the cumulative shear strain exhibit non-dissipative characteristics during deformation. Consequently, the ensuing state equations are derived for the Cauchy stress tensor and higher order stress vector.

$$\underset{\sim}{\sigma} = \rho\frac{\partial\psi}{\partial\underset{\sim}{\varepsilon}^{\mathrm{e}}} = \underset{\approx}{C} : \underset{\sim}{\varepsilon}^{\mathrm{e}} \tag{14}$$

$$\underline{M}^{\alpha} = \rho\frac{\partial\psi}{\partial\underline{Q}^{\alpha}} = A\underline{Q}^{\alpha} \tag{15}$$

When the Eq. (15) is substituted into the higher order balance equation, Eq. (8), it results in the following equation where cumulative shear strain directly links to the scalar higher order stress.

$$S^{\alpha} = \nabla.\underline{M}^{\alpha} = A\Delta\gamma^{\alpha}_{\mathrm{cum}} \tag{16}$$

Consequently, the residual dissipation during deformation is determined by the dissipative powers encompassed within the Clausius-Duhem inequality.

$$\mathcal{D}^{\alpha} = \left|\tau^{\alpha}\right|\dot{\gamma}^{\alpha} - \left(\tau^{\alpha}_{\mathrm{cr}} - S^{\alpha}\right)\dot{\gamma}^{\alpha}_{\mathrm{cum}} \geq 0 \tag{17}$$

Within this context, $\tau^{\alpha} = \underset{\sim}{\sigma} : \left(\underline{s}^{\alpha} \otimes \underline{m}^{\alpha}\right)$ represents the resolved shear stress, while the critical resolved shear stress, denoted as $\tau^{\alpha}_{\mathrm{cr}}$, is defined by $\tau^{\alpha}_{\mathrm{cr}} = \rho\frac{\partial\psi^{h}}{\partial\gamma^{\alpha}_{\mathrm{cum}}}$ and is regarded as the thermodynamic driving force. The dissipation potential is established as $\Omega^{\alpha} = \Omega\left(\tau^{\alpha}, \tau^{\alpha}_{\mathrm{cr}} - S^{\alpha}\right)$. Additionally, the Schmid yield function is assumed to take the form of $f^{\alpha} = \left|\tau^{\alpha}\right| - \left(\tau^{\alpha}_{\mathrm{cr}} - S^{\alpha}\right)$ and carries following relations with the evolution of the flow rule and cumulative shear strain.

$$\dot{\gamma}^{\alpha} = \frac{\partial\Omega^{\alpha}}{\partial\tau^{\alpha}} = \mathrm{sign}\left(\tau^{\alpha}\right)\frac{\partial\Omega^{\alpha}}{\partial f^{\alpha}} \tag{18}$$

$$\dot{\gamma}^{\alpha}_{\mathrm{cum}} = -\frac{\partial\Omega^{\alpha}}{\partial\left(\tau^{\alpha}_{\mathrm{cr}} - S^{\alpha}\right)} = \frac{\partial\Omega^{\alpha}}{\partial f^{\alpha}} = \left|\dot{\gamma}^{\alpha}\right| \tag{19}$$

In order to ensure non-negativity of dissipation during deformation, the dissipation potential must satisfy the condition $\frac{\partial\Omega^{\alpha}}{\partial f^{\alpha}} > 0$. Since rate-independent crystal plasticity theories often lead to ill-posed conditions (Miehe and Schröder, 2001; Forest and Rubin, 2016), particularly concerning the selection of active slip systems which require additional computational considerations, a rate-dependent viscoplastic deformation approach is adopted here to address these numerical issues. Consequently, a viscoplastic power-law potential, characterized by the Norton flow coefficient, K, Norton flow exponent, n, and Macaulay bracket,[3] is chosen for the dissipation potential.

$$\Omega^{\alpha}\left(\tau^{\alpha}, \tau^{\alpha}_{\mathrm{cr}} - S^{\alpha}\right) = \frac{K}{n+1}\left\langle\frac{f^{\alpha}\left(\tau^{\alpha}, \tau^{\alpha}_{\mathrm{cr}} - S^{\alpha}\right)}{K}\right\rangle^{n+1} = \frac{K}{n+1}\left\langle\frac{\left|\tau^{\alpha}\right| - \tau^{\alpha}_{\mathrm{cr}} + S^{\alpha}}{K}\right\rangle^{n+1} \tag{20}$$

Therefore, the shear strain evolution is derived by the Eq. (18) and the critical resolved shear stress is chosen to take the form of the exponential of the cumulative shear strain associated with each slip system to trigger the localization due to softening. Such exponential softening corresponds to the interactions between dislocations and hardening defects caused by neutron irradiation, such as Frank loops, and their subsequent annihilation, resulting in the formation of localized softened regions inside the grains.

[2] In general, each slip system α can be associated with different A^{α}, however, a single non-local parameter ($A^{\alpha} = A$) is employed here.

[3] Which yields zero for negative argument value and the value itself when it is positive.

$$\dot{\gamma}^{\alpha} = \text{sign}\left(\tau^{\alpha}\right)\left\langle \frac{\left|\tau^{\alpha}\right| - \tau^{\alpha}_{\text{cr}} + S^{\alpha}}{K} \right\rangle^{n} \tag{21}$$

$$\tau^{\alpha}_{\text{cr}} = \tau^{\alpha}_{0} - \triangle\tau^{\alpha}\left[1 - \exp\left(-\frac{\gamma^{\alpha}_{cum}}{\gamma_0}\right)\right] + H^{\alpha}\gamma^{\alpha}_{cum} \tag{22}$$

Here, τ^{α}_{0} represents the initial critical resolved shear stress, H^{α} indicates the hardening modulus, $\triangle\tau^{\alpha}$ denotes the maximum softening parameter, and γ_0 serves as a parameter controlling the softening rate. These parameters are instrumental in calibrating physics-based irradiation models and the effects of various irradiation doses. A comprehensive discussion on the physical interpretation of higher order stresses, their correlation with Nye's tensor, and the determination of the specific range for the non-local parameter is provided in Appendix A. Furthermore, the calibration of the material parameters within the proposed model, in relation to the dislocation-based crystal plasticity framework, is detailed in Appendix B.

Furthermore, the lattice rotation angle resulting from elastic distortion is taken into consideration to distinguish between the two types of localization bands (slip and kink bands). Both types of bands are localized in the plastic part of the deformation, but they exhibit different elastic behaviors. Consequently, the polar decomposition of the elastic part of the deformation gradient tensor is utilized to calculate the rotation tensor and rotation angle by the elastic part of deformation (Marano et al., 2019).

$$\underset{\sim}{F}^{\text{e}} = \underset{\sim}{1} + (\nabla \underline{u})^{\text{e}} = \underset{\sim}{R}^{\text{e}}.\underset{\sim}{U}^{\text{e}} \tag{23}$$

$$\theta = \arccos\left(\frac{1}{2}\left(\text{tr}(\underset{\sim}{R}^{\text{e}}) - 1\right)\right) \tag{24}$$

This SGCP model introduces higher order traction, m^{α}, which is evaluated based on the gradient of cumulative shear strain. This traction is utilized when applying higher order boundary conditions to analyze the influence of grain boundaries on localization patterns in polycrystalline aggregates. In this context, the study considers the most well-known higher order boundary conditions,[4] which have previously been reported in terms of MicroContinuity (Marano et al., 2021), MicroFree (Cermelli and Gurtin, 2002), and MicroHard (Lebensohn and Needleman, 2016). These higher order boundary conditions are directly applied to the voxels that come into contact with the grain boundaries, a process automated through an in-house code. For instance, in the MicroFree boundary condition, the higher order traction on the grain boundary is set[5] to zero ($m^{\alpha} = 0$), reflecting a scenario in which all dislocations arriving at the grain boundaries are freely transmitted, without encountering resistance, to the neighboring grain. This boundary condition is implemented in the code by setting the non-local parameter to zero for the voxels located on each side of the grain boundaries, as illustrated by the following equation:

$$A = 0 \quad \forall \underline{x} \in \text{grain boundary} \tag{25}$$

In addition, the MicroHard boundary condition signifies that plastic shear strain does not transmit to the neighboring grains or dislocations stop on grain boundary. This condition is implemented by assigning an exceptionally high critical resolved shear stress value to the voxels situated on the grain boundaries,[6] as expressed by the equation:

$$\tau^{\alpha}_{\text{cr}} = 10^{5}\ \tau^{\alpha}_{0} \quad \forall \underline{x} \in \text{grain boundary},\ \forall \alpha \in N_{\alpha} \tag{26}$$

Lastly, the MicroContinuity boundary condition interprets that the higher order scalar traction ($m^{\alpha}\#$) remains continuous[7] on both sides of the grain boundary, and its implementation does not require any modifications to the constitutive equations due to establishing finite difference scheme in Fourier space described in the next section.

2.2. FFT-homogenization method

The FFT-homogenization method is employed for the numerical solution of the SGCP model discussed in the preceding section. The computational framework includes the solution of both balance equations: the classical linear momentum balance equation (Cauchy equation of motion Eq. (7)) and the higher order balance equation, Eq. (8), which are explicitly coupled and integrated into a fixed-point iterative algorithm. Initially, the algorithm solves the classical linear momentum balance equation iteratively until the desired tolerance is reached (Table 1: Steps 3–13). Subsequently, the higher order stress is determined using the cumulative shear strain from the first part of the algorithm through a finite difference scheme (Table 1: Step 14). Within this algorithm, a periodic microstructure of the material, enclosed within a volume denoted as $V = L_1 \times L_2 \times L_3$, is discretized into a regular square grid composed of voxels, with a total of $N^{\text{tot}} = N_1 \times N_2 \times N_3$ voxels in each Cartesian direction. In the Fourier space, the discretized frequency is expressed in relation to the dimensions of the lattice and grid resolution. Particularly, if the grid resolution is even, the frequency is determined by the following expression (Moulinec and Suquet, 1998).

$$\xi_i = \frac{2\pi m_i}{L_i}, \qquad m_i = 1 - \frac{N_i}{2}, 2 - \frac{N_i}{2}, \ldots, 0, \ldots, \frac{N_i}{2} - 1, \frac{N_i}{2} \tag{27}$$

[4] The higher order traction expression used in this study differs from those cited; hence, its interpretations differ, despite sharing the same name.

[5] $\underline{M}^{\alpha} = \underline{0} \Rightarrow m^{\alpha} = 0$.

[6] This boundary condition type is interpreted in this study as a result of the corrosive environment in reactor conditions. Hydrogen and oxygen diffusion towards the grain boundary renders it brittle and thicker, which makes the transition of dislocations less likely.

[7] Also $\underline{M}^{\alpha}\#$.

Table 1
Pseudo code of the FFT-Algorithm.

1 Extrapolation of the displacement gradient tensor at new time step $\nabla \underset{\sim}{u}^{i}(t_n + \Delta t_n) = \nabla \underset{\sim}{u}(t_n) + \frac{\Delta t_n}{\Delta t_{n-1}} \left[\nabla \underset{\sim}{u}(t_n) - \nabla \underset{\sim}{u}(t_{n-1})\right]$
2 Implicit time integration of state variables: Appendix E
3 FFT-algorithm: New iteration (i+1)
4 Convergence test: linear momentum balance equation (Eq. (42))
5 Polarization tensor field: Evaluation in real space $\underset{\sim}{\tau}^{i}(\underline{x}) = \underset{\sim}{\sigma}^{i}(\underline{x}) - \underset{\approx}{C}^{0} : \nabla \underline{u}^{i}(\underline{x})$
6 Polarization tensor: Transform to Fourier space $\widehat{\underset{\sim}{\tau}}^{i}(\underline{\xi}) = \mathcal{FFT}\left(\underset{\sim}{\tau}^{i}\right)$
7 Tensile loading: Mixed boundary condition (Eqs. (40), (41))
8 Displacement gradient tensor: Evaluation in Fourier space for new iteration $\widehat{\nabla \underline{u}}^{i+1}(\underline{\xi}) = -\widehat{\underset{\approx}{\Gamma}}^{M} : \widehat{\underset{\sim}{\tau}}^{i}(\underline{\xi}) \qquad \forall \underline{\xi} \neq \underline{0}$ $\widehat{\nabla \underline{u}}^{i+1}(\underline{0}) = \overline{\nabla \underline{u}}^{i} \qquad \underline{\xi} = \underline{0}$
9 Displacement gradient tensor: Inverse transform to real space $\nabla \underline{u}^{i+1}(\underline{x}) = \mathcal{IFFT}\left(\widehat{\nabla \underline{u}}^{i+1}(\underline{\xi})\right)$
10 Anderson Acceleration
10.1 Displacement gradient tensor: Saved
10.2 Apply every three iterations $(i + 1/3 == 3k, \quad k = 1, 2, 3, \ldots)$
11 Implicit time integration of state variables: Appendix E
12 Convergence tests: mixed boundary conditions (Eqs. (43), (44))
13 If all convergence tests satisfy the tolerances
13.1 Yes: Go to step 14
13.2 No: Go to step 3
14 Higher order balance equation
14.1 Cumulative shear strain: Transform to Fourier space $\widehat{\gamma^{a}_{cum}} = \mathcal{FFT}\left(\gamma^{a}_{cum}\right)$
14.2 Higher order stress: Evaluating in Fourier space $\widehat{S^{a}}(\underline{\xi}) = A \ \hat{A} \ \widehat{\gamma^{a}_{\text{cum}}}$
14.3 Higher order stress: Inverse transform to real space $S^{a}(\underline{x}) = \mathcal{IFFT}\left(\widehat{S^{a}}(\underline{\xi})\right)$
15 Updating time step

The Lippmann–Schwinger equation (Lippmann and Schwinger, 1950) is derived through the additive decomposition of the total displacement gradient tensor into its average and fluctuation parts, Eq. (28), with the assumption that the fluctuation term exhibits periodic behavior ($\nabla \underline{u}^{\star} \# \partial\mathcal{B}$) while the traction vector displays anti-periodic ($\underset{\sim}{\sigma}.\underline{n} - \# \partial\mathcal{B}$) characteristics at the boundary of the microstructure. To incorporate the effect of the elastic deformation-induced rotation within the framework of infinitesimal strain, the Lippmann–Schwinger equation is expressed in terms of the displacement gradient tensor rather than the symmetric infinitesimal strain tensor. This modification is of particular importance in the present study because it enables the consideration of the non-symmetric part of the displacement gradient, thereby facilitating the calculation of the lattice rotation angle, Eq. (24), attributable to the elastic part of the total deformation, as previously reported (Marano et al., 2021).

$$\nabla \underline{u}(\underline{x}) = \overline{\nabla \underline{u}} + \nabla \underline{u}^{\star}(\underline{x}) \qquad \forall \underline{x} \in \mathcal{B}, \ \nabla \underline{u}^{\star} \# \partial\mathcal{B} \tag{28}$$

$$\underset{\sim}{\sigma}(\underline{x}) = \underset{\approx}{C}(\underline{x}) : \nabla \underline{u}(\underline{x}) \qquad \forall \underline{x} \in \mathcal{B}, \ \ \underset{\sim}{\sigma}.\underline{n} - \# \partial\mathcal{B} \tag{29}$$

$$\underset{\sim}{\tau}(\underline{x}) = \underset{\sim}{\sigma}(\underline{x}) - \underset{\approx}{C}^{0} : \nabla \underline{u}(\underline{x}) \quad \forall \underline{x} \in \mathcal{B} \tag{30}$$

$$\nabla . \left(\underset{\sim}{\sigma}(\underline{x})\right) = \underline{0} \qquad \forall \underline{x} \in \mathcal{B} \tag{31}$$

Hence, the solution in both real space and Fourier space is acquired by performing the convolution (in real space) and double contraction (in Fourier space) between the Green operator, denoted as ($\underset{\approx}{\Gamma}$), and the polarization tensor, represented as $\underset{\sim}{\tau}$:

$$\text{Real space:} \qquad \nabla \underline{u}^{\text{tot}}(\underline{x}) = -\underset{\approx}{\Gamma} * \underset{\sim}{\tau}(\underline{x}) \tag{32}$$

$$\text{Fourier space:} \qquad \begin{cases} \widehat{\nabla \underline{u}}^{\text{tot}}(\underline{\xi}) = -\widehat{\underset{\approx}{\Gamma}}(\xi) : \widehat{\underset{\sim}{\tau}}(\underline{\xi}) & \forall \underline{\xi} \neq \underline{0} \\ \widehat{\nabla \underline{u}}^{\text{tot}}(\underline{0}) = \overline{\nabla \underline{u}} & \underline{\xi} = \underline{0} \end{cases} \tag{33}$$

To enhance the accuracy, the algorithm employs the rotated scheme together with an auxiliary isotropic homogeneous medium, $\underset{\approx}{C}^{0}$, to compute the modified Green operator. This choice effectively mitigates oscillations in the Fourier space, even in regions with

high contrast, as it is well-documented for its superior accuracy in handling local fields (Willot, 2015). Additionally, it is noteworthy that this Green operator is both general and non-symmetric, ensuring consistency with the non-symmetric displacement gradient.

$$\underset{\approx}{\hat{\Gamma}}^{M} = \underline{f}^{R} \otimes \left[\underline{f}^{R}.\underset{\approx}{C}^{0}.\underline{f}^{R'}\right]^{-1} \otimes \underline{f}^{R'} \tag{34}$$

Here, the $\underline{f}^{R}$ and $\underline{f}^{R'}$ are modified frequencies respectively corresponding to the gradient and divergence operators in this rotated scheme, Eq. (35), and centered scheme, Eq. (36), are determined as follows (Willot, 2015):

$$f_i^R = \frac{\mathrm{j}}{4}\tan\left(\frac{\xi_i}{2}\right)\left(1+\exp\left(\mathrm{j}\xi_1\right)\right)\left(1+\exp\left(\mathrm{j}\xi_2\right)\right)\left(1+\exp\left(\mathrm{j}\xi_3\right)\right) \tag{35}$$

$$f_i^C = \mathrm{j}\sin\left(\xi_i\right) \tag{36}$$

where j is the imaginary complex unit. Moreover, the fixed-point algorithm is enhanced with Anderson acceleration. This augmentation serves the dual purpose of circumventing the need for calculating the tangent operator in nonlinear material behavior and accelerating the convergence process. In particular, this study opts for the Anderson acceleration method known as "alternate $2-\delta$", Appendix C, due to its documented superior performance as reported in a previous study (Ramière and Helfer, 2015).

Upon achieving the desired level of accuracy in solving the linear momentum balance equation in the first part of the algorithm (Table 1: Step 13), the cumulative shear strain serves as the input for the higher order balance equation (or evaluating the higher order stress Eq. (16)) stemming from the SGCP model. Within this algorithm, the cumulative shear strain variable is transformed into the Fourier space (Table 1: Step 14.1) and subsequently subjected to multiplication by the Laplacian operator and non-local parameter (Table 1: Step 14.2). While the MicroFree boundary condition is applied within the Fourier space, Eq. (25), the MicroHard boundary condition is implemented in the real space, Eq. (26). The last step consists of the transformation of higher order stress back into the real space via the inverse Fourier transform (Table 1: Step 14.3). In this study, the 21-voxel differentiation scheme is employed to evaluate the Laplacian operator in the Fourier space which provides better performance compared to the 9-voxel differentiation scheme (Marano et al., 2021; Lebensohn and Needleman, 2016) in the discontinuous regions like grain boundary. Both schemes were compared in a previous study considering an elastic material with inclusion (Neumann et al., 2002). Since this operator is evaluated only once throughout the entire simulation, it is worth noting that both finite difference schemes have equal computational costs.[8]

$$\hat{\Delta} = \begin{cases} \sum_i \frac{2}{dx_i^2}\left[\cos\left(\xi_i\right)-1\right] + \mathrm{O}(dx_i^2) & \text{9-voxel scheme} \\ \sum_i \frac{1}{6dx_i^2}\left[-\cos\left(2\xi_i\right)+16\cos\left(\xi_i\right)-15\right] + \mathrm{O}(dx_i^4) & \text{21-voxel scheme} \end{cases} \tag{37}$$

In particular, this operator together with the non-local parameter are multiplied with the cumulative shear strain in the Fourier space to evaluate the higher order stress and return to the real space by the inverse Fourier transform.

$$S^{\alpha} = \mathcal{IFFT}\left(A\ \hat{\Delta}\ \widehat{\gamma^{\alpha}_{\mathrm{cum}}}\right) \tag{38}$$

Furthermore, when tensile loading is taken into account in simulations, a mixed boundary condition is applied when solving the classical linear momentum balance equation (Table 1: Step 7). This boundary condition requires simultaneous control over both the macroscopic displacement gradient tensor and the macroscopic Cauchy stress tensor. Specifically, to model tensile loading along the y-direction, the macroscopic displacement gradient tensor along the y-direction is constrained, while the macroscopic stress in the other directions is maintained at zero to permit unrestricted deformation of the microstructure in those directions. These boundary conditions are assigned at zero frequency in Fourier (complex) space, corresponding to the macroscopic behavior. Higher frequencies within the Green operator and polarization tensor govern the microscopic behavior.

$$\begin{cases} \left(\widehat{\nabla\underline{u}}\right)_{ij}(\underline{0}) = \left(\overline{\nabla\underline{u}}\right)_{ij} & \text{if } ij = 22 \\ \left(\underset{\sim}{\bar{\sigma}}\right)_{ij} = 0 & \text{if } ij \neq 22 \end{cases} \tag{39}$$

The macroscopic displacement gradient tensor is initially imposed as an input but is subjected to modification during the fixed-point iterations (Table 1: Step 7 and Eq. (40)). In addition, the arc-length method is employed, as it has been previously reported to offer enhanced performance when dealing with strongly nonlinear constitutive equations (Michel et al., 1999). In this method, only the direction of the loading is enforced using an auxiliary parameter associated with the arc-length method; for tensile loading in y-direction denoted as $\underset{\sim}{\Sigma}^{0} = \underline{e}_2 \otimes \underline{e}_2$. Subsequently, the components of the displacement gradient tensor are derived in terms of the displacement gradient tensor from the previous iteration, the Cauchy stress tensor from the previous iteration, the unknown level of the overall stress parameter (k^i), and the direction of the loading.

$$\overline{\nabla\underline{u}}^{i} = \overline{\nabla\underline{u}}^{i-1} + \left[\underset{\approx}{C}^{0}\right]^{-1} : \left(k^i \underset{\sim}{\Sigma}^{0} - \underset{\sim}{\bar{\sigma}}^{i-1}\right) \tag{40}$$

$$k^i = \frac{\overline{\nabla\underline{u}}^{i-1} : \underset{\sim}{\Sigma}^{0} + \underset{\sim}{\Sigma}^{0} : \left(\left[\underset{\approx}{C}^{0}\right]^{-1} : \underset{\sim}{\bar{\sigma}}^{i-1} - \overline{\nabla\underline{u}}^{i-1}\right)}{\underset{\sim}{\Sigma}^{0} : \left[\underset{\approx}{C}^{0}\right]^{-1} : \underset{\sim}{\Sigma}^{0}} \tag{41}$$

[8] More details in Appendix D.

To ensure the accuracy of the results, the algorithm incorporates three convergence tests. These tests are established for the linear momentum balance equation (Moulinec and Suquet, 1998), macroscopic stress (Joëssel et al., 2018), and macroscopic displacement gradient tensor (Nguyen, 2010). In all simulations, a tolerance Tol = 10^{-4} is specified to satisfy the convergence criteria.

$$\text{test}^{i}_{\text{Cauchy}} = \frac{\left(\frac{1}{N^{tot}} \sum_d \| \underline{f}'_d . \widehat{\underset{\sim}{\sigma}}(\underline{\xi}_d) \|^2\right)^{1/2}}{\| \widehat{\underset{\sim}{\sigma}}(\underline{0}) \|} < \text{Tol} \tag{42}$$

$$\text{test}^{i}_{\text{Stress Mac}} = \frac{\| \underset{\sim}{\bar{\sigma}}^{i}(\underline{0}) - k^i \underset{\sim}{\Sigma}^0 \|}{\| k^i \underset{\sim}{\Sigma}^0 \|} < \text{Tol} \quad \left\{ \forall ij | \sigma_{ij} \neq \text{tensile direction} \right\} \tag{43}$$

$$\text{test}^{i}_{\text{Displacement Mac}} = \frac{\| \widehat{\overline{\nabla \underline{u}}}^{i}(\underline{0}) - \overline{\nabla \underline{u}} \|}{\| \widehat{\overline{\nabla \underline{u}}}^{i}(\underline{0}) \|} < \text{Tol} \quad \left\{ \forall ij | \nabla \underline{u}_{ij} = \text{tensile direction} \right\} \tag{44}$$

where $\| \ \|$ represents the Euclidean norm of tensor. The overall pseudo code[9] of the FFT algorithm is presented in Table 1 and details of time integration are provided in Appendix E. Superior performance of the code due to introduced improvements in the fixed-point iteration of the FFT algorithm in the proposed SGCP model is demonstrated in Appendix F.

3. Results

The results compose the validation of the FFT-homogenization algorithm concerning the developed analytical analysis for different material behaviors, as well as simulations and visualizations of slip and kink bands within single crystal and polycrystalline simulations. In all simulations except Section 3.4, two-dimensional periodic microstructures with a single voxel thickness along the $\underline{e}_3$ basis vector are considered, which corresponds to an infinite 3-dimensional columnar microstructure along the $\underline{e}_3$ direction. The choice to simulate in 2 dimensions is motivated by the objective of tracking and visualizing the path of localization bands more effectively, as well as observing the transmission of these bands along the grain boundaries.

3.1. Analytical solution of the MicroSlip SGCP model

Previous studies have derived analytical solutions based on their generalized continua models. For instance, (Cordero et al., 2010) proposed analytical solutions for the Cosserat continuum and MicroCurl SGCP of a two-phase periodic microstructure. The MicroCurl SGCP was further developed into the shear band problems (Marano et al., 2021). Additionally, (Scherer et al., 2019) developed micromorphic crystal plasticity. Inspired by these studies, analytical solutions for the proposed MicroSlip SGCP model, accounting for different material behaviors, are developed and presented in this section.

In this context, a single crystal that is unbounded in the y-direction is considered, Fig. 1. The crystal is subjected to shear loading, $\bar{\gamma}$, and is capable of exhibiting elasto-plastic behavior through a single slip system ($N_\alpha = 1$), which is oriented in the direction of the Cartesian basis ($\underline{e}_1, \underline{e}_2$). The elastic behavior conforms to the linear isotropic case, Eq. (49), while plastic deformation is accompanied by linear rate-independent type associated with cumulative shear strain, Eq. (50). Consequently, the following equations are presented in accordance with the requirements of the MicroSlip SGCP model.

$$\underline{u}^{\text{tot}} = u(x_1)\underline{e}_2 \tag{45}$$

$$(\nabla \underline{u})^{\text{tot}} = \frac{\partial u}{\partial x_1} \underline{e}_2 \otimes \underline{e}_1 \tag{46}$$

$$(\nabla \underline{u})^{\text{p}} = \gamma_{cum} \underline{e}_1 \otimes \underline{e}_2 \tag{47}$$

$$(\nabla \underline{u})^{\text{e}} = \frac{\partial u}{\partial x_1} \underline{e}_2 \otimes \underline{e}_1 - \gamma_{cum} \underline{e}_1 \otimes \underline{e}_2 \tag{48}$$

$$\underset{\sim}{\sigma} = \mu \left(\frac{\partial u}{\partial x_1} - \gamma_{cum} \right) \left(\underline{e}_1 \otimes \underline{e}_2 + \underline{e}_2 \otimes \underline{e}_1 \right) \tag{49}$$

$$\tau_{\text{cr}} = \tau_0 + H \gamma_{cum} \tag{50}$$

$$S = A \frac{\partial^2 \gamma_{cum}}{\partial x_1^2} \tag{51}$$

The resolved shear stress corresponding to this slip system equals the shear component of the Cauchy stress tensor, as the slip system is parallel to the Cartesian basis.

$$\tau = \underset{\sim}{\sigma} : \left(\underline{e}_1 \otimes \underline{e}_2 \right) = \sigma_{12} \tag{52}$$

The linear momentum balance equation results in a uniform distribution of both the Cauchy stress tensor and the resolved shear stress due to the absence of body and inertial forces.

$$\nabla . \underset{\sim}{\sigma} = \underline{0} \Rightarrow \frac{\partial \sigma_{12}}{\partial x_2} = \frac{\partial \tau}{\partial x_2} = 0 \tag{53}$$

[9] The arrangement of different parts of the fixed-point iteration, along with optimal choices for various steps, is the main novelty of the proposed FFT-algorithm in the SGCP model.

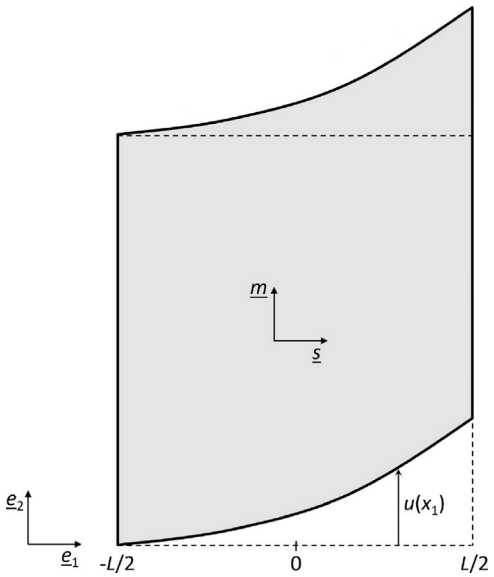

Fig. 1. Single crystal under shear loading.

The yield function in the elasto-plastic region of the crystal provides a differential equation of cumulative shear strain, which is written in the following expression:

$$\left|\tau\right| - \tau_{\mathrm{cr}} + S = 0 \Rightarrow \frac{\partial^2 \gamma_{cum}}{\partial x_1^2} - \frac{H}{A}\gamma_{cum} + \frac{\tau - \tau_0}{A} = 0 \tag{54}$$

3.1.1. Linear hardening ($H > 0$)

By introducing the new constant $\lambda_0 = \sqrt{\frac{A}{H}}$, the differential equation, Eq. (54), is transformed as follows:

$$\frac{\partial^2 \gamma_{cum}}{\partial x_1^2} - \frac{1}{\lambda_0^2}\gamma_{cum} + \frac{\tau - \tau_0}{\lambda_0^2 H} = 0 \tag{55}$$

The differential equation, Eq. (55), possesses a single non-trivial general solution in the form of hyperbolic sine and cosine functions in the case of hardening ($H > 0$).

$$\gamma_{cum}\left(x_1\right) = \alpha \cosh\left(\frac{x_1}{\lambda_0}\right) + \beta \sinh\left(\frac{x_1}{\lambda_0}\right) + \frac{\tau - \tau_0}{H} \tag{56}$$

By taking into account the symmetry condition regarding shear strain with respect to the Cartesian basis $\underline{e}_1$, the coefficient β becomes zero, and imposing the microhard boundary condition at the boundary of the elasto-plastic crystal, the coefficient α becomes:

$$\gamma_{\mathrm{cum}}(\pm\tfrac{L}{2}) = 0 \Rightarrow \alpha = -\frac{\tau - \tau_0}{H \cosh\left(\frac{L}{2\lambda_0}\right)} \tag{57}$$

By substituting these coefficients into the Eq. (56), the solution reduces to the following expression:

$$\gamma_{\mathrm{cum}}(x_1) = \frac{\tau - \tau_0}{H}\left[1 - \frac{\cosh\left(\frac{x_1}{\lambda_0}\right)}{\cosh\left(\frac{L}{2\lambda_0}\right)}\right] \tag{58}$$

Therefore, the only remaining variable that needs to be determined to fully obtain the solution is the resolved shear stress. This variable can be determined by integrating the shear strain over the domain and subtracting it from the total applied shear loading ($\bar{\gamma}$).

$$\tau = \mu\left[\bar{\gamma} - \tfrac{1}{L}\int_{-L/2}^{L/2} \gamma_{\mathrm{cum}}(x_1)dx_1\right] = \mu[\bar{\gamma} + \frac{\tau - \tau_0}{\frac{HL}{2\lambda_0 \tanh\left(\frac{L}{2\lambda_0}\right) - 1}}] \Rightarrow \tag{59}$$

$$\tau = \frac{\bar{\gamma} - \frac{\tau_0}{\frac{HL}{2\lambda_0 \tanh\left(\frac{L}{2\lambda_0}\right) - 1}}}{\frac{1}{\mu} - \frac{2\lambda_0 \tanh\left(\frac{L}{2\lambda_0}\right) - 1}{HL}} \tag{60}$$

3.1.2. Perfect plasticity ($H = 0$)

In the case of perfect plasticity, $H = 0$, the differential equation, Eq. (54), transforms into the following equation:

$$\frac{\partial^2 \gamma_{\text{cum}}}{\partial x_1^2} = \frac{\tau_0 - \tau}{A} \tag{61}$$

The non-trivial general solution takes the form of a parabola:

$$\gamma_{\text{cum}}\left(x_1\right) = \frac{\tau_0 - \tau}{2A} x_1^2 + \alpha x_1 + \beta \tag{62}$$

Applying the boundary condition leads to the determination of the two unknown constants.

$$\begin{cases} \text{Symmetry condition: } \alpha = 0 \\ \text{Micro hard boundary on the boundary: } \beta = \frac{\tau - \tau_0}{2A}(\frac{L}{2})^2 \end{cases} \tag{63}$$

As a result, the cumulative shear strain and resolved shear stress are acquired.

$$\gamma_{\text{cum}}\left(x_1\right) = \frac{\tau - \tau_0}{2A}\left[(\tfrac{L}{2})^2 - x_1^2\right] \tag{64}$$

$$\tau = \mu\left[\overline{\gamma} - \frac{1}{L}\int_{-\frac{L}{2}}^{\frac{L}{2}} \gamma_{\text{cum}}\left(x_1\right) dx_1\right] = \mu\left[\overline{\gamma} - \tfrac{\tau - \tau_0}{12A} L^2\right] \Rightarrow$$

$$\tau = \frac{\overline{\gamma} + \frac{\tau_0}{\frac{12A}{L^2}}}{\frac{1}{\mu} + \frac{L^2}{12A}} \tag{65}$$

3.1.3. Linear softening ($H < 0$)

In the context of softening behavior, the differential equation, Eq. (54), is of the elliptic type, which transforms into the following equation by introducing new constant (λ_0'):

$$\frac{\partial^2 \gamma_{\text{cum}}}{\partial x_1^2} + \frac{4\pi^2}{\lambda_0'^2}\gamma_{\text{cum}} + \frac{4\pi^2}{\lambda_0'^2}\frac{\tau - \tau_0}{|H|} = 0; \quad \lambda_0' = 2\pi\sqrt{\frac{A}{|H|}} \tag{66}$$

The non-trivial general solution to this differential equation is given by the following expression:

$$\gamma_{\text{cum}}\left(x_1\right) = \alpha\cos\left(\tfrac{2\pi x_1}{\lambda_0'}\right) + \beta\sin\left(\tfrac{2\pi x_1}{\lambda_0'}\right) + \frac{\tau - \tau_0}{H} \tag{67}$$

The symmetry condition leads to the determination of the coefficient $\beta = 0$. Additionally, owing to the localization resulting from softening behavior and instability at the onset of yield stress, it is anticipated that shear strain becomes localized within a region of width ω. Consequently, beyond this localized region, the cumulative shear strain attributed to plastic deformation is set to zero as a boundary condition. On the other hand, instead of applying the microhard boundary condition at the crystal's boundary, a vanishing higher order traction is imposed at the boundary of this localized region as an additional boundary condition.

$$\begin{cases} \text{Localization condition:} \quad \gamma_{\text{cum}}(\pm\frac{\omega}{2}) = 0 \\ \text{Higher order traction:} \quad m(\pm\frac{\omega}{2}) = \underline{M}(\pm\frac{\omega}{2}).\underline{n} = 0 \Rightarrow \frac{\partial \gamma_{\text{cum}}}{\partial x_1}|_{x_1 = \frac{\omega}{2}} = 0 \end{cases} \tag{68}$$

These boundary conditions give the expressions for both the width of shear strain localization and the final coefficient.

$$\begin{cases} \alpha = \frac{\tau - \tau_0}{H} \\ \omega = \lambda_0' = 2\pi\sqrt{\frac{A}{|H|}} \end{cases} \tag{69}$$

Hence, the solution is derived as:

$$\gamma_{\text{cum}}(x_1) = \frac{\tau - \tau_0}{H}\left[1 + \cos\left(\tfrac{2\pi x_1}{\lambda_0'}\right)\right] \tag{70}$$

The resolved shear stress is determined by evaluating the integral over the entire crystal.

$$\tau = \mu[\overline{\gamma} - \frac{1}{L}\int_{-\frac{\omega}{2}}^{\frac{\omega}{2}} \gamma_{\text{cum}}(x_1)dx_1] = \mu[\overline{\gamma} - \frac{\omega[\tau - \tau_0]}{HL}] \Rightarrow$$

$$\tau = \frac{\overline{\gamma} + \frac{\lambda_0'\tau_0}{LH}}{\frac{1}{\mu} + \frac{\lambda_0'}{LH}} \tag{71}$$

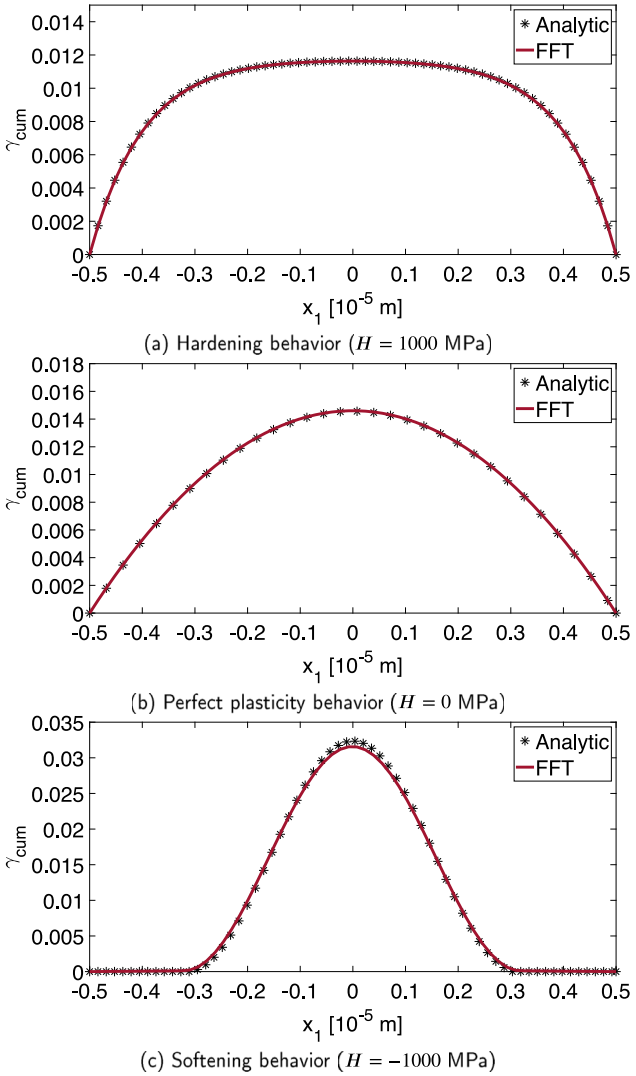

Fig. 2. Comparison of numerical and analytical results.

3.2. Comparison with analytical solutions

In this section, the numerical results from FFT-homogenization algorithm are compared with the analytical solutions in Section 3.1. To do this comparison, an infinite two-dimensional single crystal with its normal direction parallel to $\underline{e}_3$ basis vector is considered. Moreover, the crystal is equipped with an in-plane slip system $(\underline{s}, \underline{m}) = (\underline{e}_1, \underline{e}_2)$ and is subjected to shear loading with an amplitude of $\overline{\gamma} = 0.01$ with a relatively small shear rate of 10^{-6} s^{-1}. To facilitate a comparison between the analytical solution and numerical results, the crystal's behavior is composed of linear isotropic elasticity, Eq. (14), and viscoplasticity, Eq. (21). In the isotropic elastic part of the deformation, the crystal is characterized by the Young's modulus of $E = 100$ GPa and Poisson's ratio of $\nu = 0.3$. In the plastic part of deformation, the crystal's behavior is modeled as rate-dependent viscoplasticity. Since the analytic solution belongs to the rate independent case, the Norton flow parameters are set to values that represent small rate dependence.

In all cases, the higher order balance equation from the SGCP model is solved using the 21-voxel finite difference scheme and same higher order interface condition as analytical solution prescribed on the crystal's boundary. Furthermore, the initial yield stress is set to $\tau_0 = 10$ MPa, and the parameters of the Norton flow rule are chosen in the range of $n = (100, 150)$ and $K = (0.5, 1)$ MPa s^{-n}. Fig. 2 shows a comparison between the analytical and numerical results for the crystal in-plane dimensions of 0.01 mm $\times$ 0.01 mm and resolution of 64×64 voxels using the non-local parameter $A = 10^{-3}$ N. Remarkably, a high degree of agreement is observed in all three cases of linear hardening, perfect plasticity, and linear softening, which validates the implementation of the fixed-point FFT-algorithm.

Fig. 3 illustrates the size effect of single crystal under simple shear loading ($\overline{\gamma} = 0.01$). To observe this effect, two single crystals of different sizes are considered: the first one with dimensions 0.01 mm$\times$$0.01$ mm and the second one with dimensions 0.1 mm$\times$$0.1$ mm.

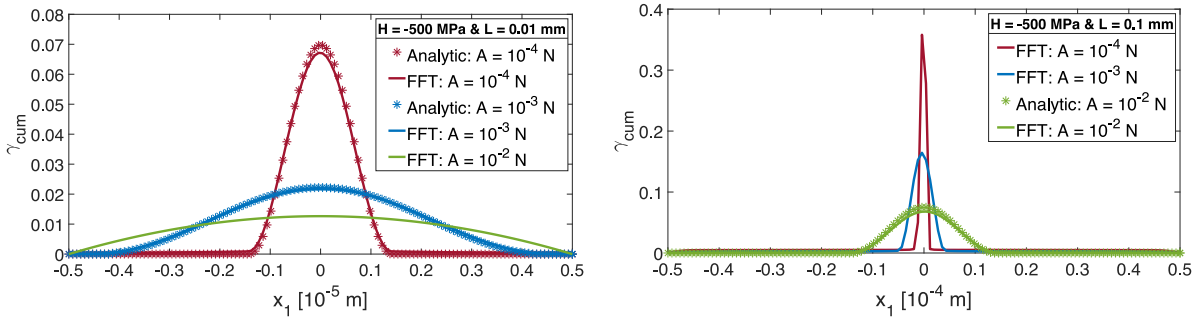

Fig. 3. Single crystal size effect on the localization band formation under simple shear loading for softening behavior ($H = -500$ MPa).

A softening modulus of $H = -500$ MPa is chosen to reproduce localization bands and demonstrate the effect of different non-local parameters on band width. The crystal properties of elastic and viscoplastic behaviors are the same[10] as those in Fig. 2. Additionally, both single crystals are discretized with a resolution of 128×128 voxels. The results from numerical simulations and analytical solutions clearly show the effect of crystal size on the amplitude and width of the localization bands under the same non-local parameter. Moreover, they explicitly demonstrate the significant effect of the non-local parameter on the regularization (smoothness) of bands in the crystals. In particular, if the amplitude of the non-local parameter meets the threshold outlined in Appendix A, the regularization process is effective, yielding stable results and appropriate band width. For instance, in a crystal with dimensions of $0.1\ \text{mm} \times 0.1\ \text{mm}$, a non-local parameter of $A = 10^{-4}$ N does not satisfy the proper threshold, resulting in an inefficient regularization process and narrow band width. Conversely, in a crystal with dimensions of $0.01\ \text{mm} \times 0.01\ \text{mm}$, a non-local parameter of $A = 10^{-2}$ N overestimates the effect of regularization and large band width. Therefore, it is concluded that selecting an appropriate amplitude for the non-local parameter ensures the correct influence of higher order stresses within the localization band. This influence is physically interpreted as the energy stored in the dislocation pile-up mechanism, detailed in Appendix A, which increases the width of the band by resisting dislocation glide.

3.3. Single crystal: regularization of localization bands and irradiation effect

In this section, a periodic single crystal with unit cell dimensions of 0.1 mm × 0.1 mm is subjected to tensile loading along the y-direction. Specifically, the applied tensile loading has a magnitude of $\overline{\nabla u}_{yy} = 0.01$ with a strain rate of $10^{-6}\ s^{-1}$ and all other components of the Cauchy stress tensor are fixed to zero. A single slip system[11] ($N_\alpha = 1$) is oriented at a 45-degree clockwise with respect to the loading direction. To trigger the localization at the center of a crystal, an imperfection or defect is deliberately placed at the central voxel $(\frac{N_1}{2}, \frac{N_2}{2})$. Namely, the critical resolved shear stress[12] on this voxel is set to $\tau_0^d = 0.99\tau_0$. The results are presented for the CCP and SGCP model, where in the latter the MicroContinuity interface condition is assumed on the unit cell boundary.

The crystal parameters for the results in Figs. 4, 5, and 6 are specified as follows. Isotropic elastic behavior is modeled by the Young modulus ($E = 100$ GPa) and Poisson ratio ($\nu = 0.3$). The Norton flow coefficient ($K = 10$ MPa s^{-n}) and exponent ($n = 15$) are chosen to represent typical viscoplastic behavior of irradiated austenitic stainless steel (Hure et al., 2016). Furthermore, the irradiation effect corresponding to local softening behavior is characterized by the initial critical resolved shear stress $\tau_0 = 100$ MPa, maximum softening parameter $\triangle\tau = 30$ MPa and softening rate $\gamma_0 = 0.05$. Also, the non-local parameter of the SGCP model is set to $A = 10^{-3}$ N and three different grid resolutions are considered for the crystal, corresponding to 40×40, 60×60, and 80×80 voxels to assess the regularization of the SGCP model. Respectively, Figs. 4, 5, and 6 depict the distributions of cumulative shear strain (γ_{cum}), absolute value of higher order stress ($|S|$), and rotation angle (θ) from the CCP and SGCP frameworks with different grid resolutions. The results from both frameworks reproduce two types of localization bands: the first being a slip band parallel to the slip direction $\underline{s}$, and the second being a kink band perpendicular to the slip direction. CCP simulations demonstrate a well-known issue in the localization problem, where the results are dependent on discretization (grid resolution). For instance, the width of the localization bands decreases or even disappears once the resolution is increased. Moreover, variables such as the cumulative shear strain and rotation angle undergo changes in amplitude. On the other hand, the results from SGCP show that the localization band width, it's amplitude and rotation angle remain constant (objective) for different grid resolutions. Additionally, SGCP results exhibit concentration (from crossing of the two bands) around the crystal defect, which is absent in the CCP. To investigate the regularization process, the corresponding higher order stress, S, is plotted in Fig. 5, revealing variations in amplitude within the localization bands while maintaining consistent width and intensity across different grid densities. In summary, the proposed SGCP model properly regulates and overcomes the localization instability in single crystal simulations.

[10] In the crystal with dimensions of $0.1\ \text{mm} \times 0.1\ \text{mm}$ larger τ_0 is used to obtain comparable band amplitudes.

[11] Employing a single slip system, in combination with the proposed FFT algorithm, is sufficient to accurately reproduce both slip and kink bands within the same grain.

[12] Slightly different strengths of the defect, $\tau_0^d = 0.995\tau_0$ or $\tau_0^d = 0.98\tau_0$, produce similar distributions for the localization bands.

Table 2
Material properties used in single crystal simulations.

Case	τ_0	$\Delta\tau$	γ_0	H	Representing
Hardening	80 MPa	0 MPa	–	200 MPa	unirradiated material
Softening-1	100 MPa	40 MPa	0.2	0 MPa	irradiated material
Softening-2	100 MPa	20 MPa	0.05	0 MPa	irradiated material
Softening-3	100 MPa	50 MPa	0.1	0 MPa	irradiated material

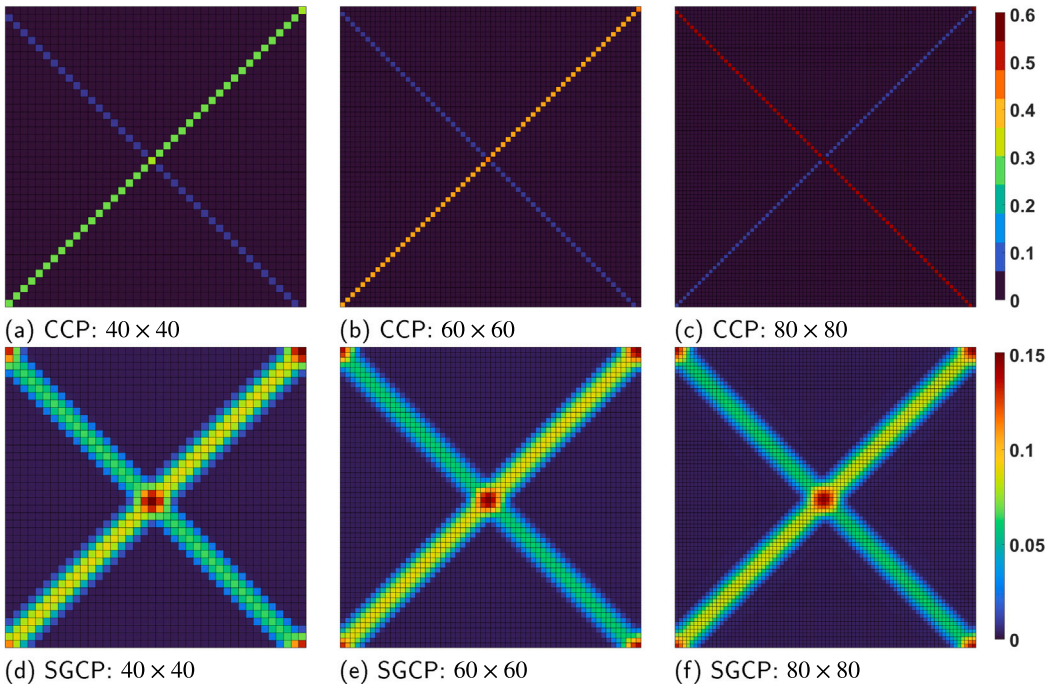

Fig. 4. Single crystal: distribution of the cumulative shear strain (γ_{cum}).

The investigation into material parameters within the proposed SGCP model, particularly in the evolution of critical resolved shear stress, is depicted in Fig. 7. This exploration involves a single crystal with identical elastic and viscoplastic parameters, loading and dimensions as the crystal in Fig. 5, measuring 0.1 mm × 0.1 mm and discretized by 128 × 128 voxels, with a defect in the center. Four sets of parameters are chosen for Eq. (22), represented as quadruples $(\tau_0, \Delta\tau, \gamma_0, H)$ defined in Table 2. The results of the hardening case are obtained using the CCP framework, while the softening results are provided by SGCP (to avoid instability) with a non-local parameter of $A = 10^{-3}$ N and MicroContinuity condition at the boundary. In the hardening case, no localization bands are produced, with a homogeneous distributions of cumulative shear strain and critical resolved shear stress. Due to hardening, the critical resolved shear stress increases from its initial amplitude ($\tau_0 = 80$ MPa). In the softening cases, all three reproduce two perpendicular localization (slip and kink) bands. The cumulative shear strain amplitudes in these bands are inversely proportional to the critical resolved shear stress, which is indicative of crystal strength. This phenomenon indicates that dislocation glide produces localized softened (weaker) bands, commonly known as clear channels in the irradiated materials such as austenitic stainless steel.

3.4. Three-dimensional single crystal

In this section, a three-dimensional face centered cubic (FCC) single crystal equipped by 12 slip systems, defined by Miller indices as $\{111\}\langle 110\rangle$, with dimensions of 1 mm × 1 mm × 1 mm is considered under tensile loading along the z-direction. The purpose of these simulations is to investigate the higher order stress, Eq. (16), associated with both localized and non-localized slip systems, as well as instabilities due to multiple slip systems activation. Therefore, a direct comparison is performed between the results obtained from the proposed FFT-algorithm and the FEM computation using the Umat-Abaqus subroutine (Simulia, 2015) to validate the CCP framework in three-dimensional crystal. To be compatible with the FFT method, periodic boundary conditions are implemented in the FE model, as briefly described here. In each Cartesian direction, $\underline{e}_i$, a reference node, P_i, is defined to constrain all nodes' displacements on the parallel boundary surfaces of the crystal, obtaining the periodic boundary condition. For example, to implement tensile loading along the z-direction, an incremental displacement, $u_z(P_i)$, is applied to the reference node. This results in non-zero macroscopic stress in the z-direction, $\langle\sigma_{33}\rangle \neq 0$, and zero macroscopic stress in other directions, $\langle\sigma_{ij}\rangle = 0$ if $ij \neq 33$. Consequently, the same periodic boundary condition as in the FFT-homogenization method is achieved.

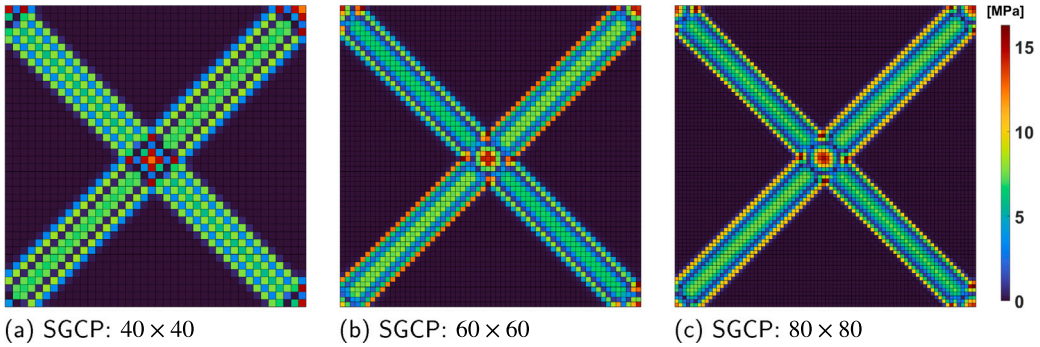

Fig. 5. Single crystal: distribution of the absolute value of the higher order stress ($|S|$).

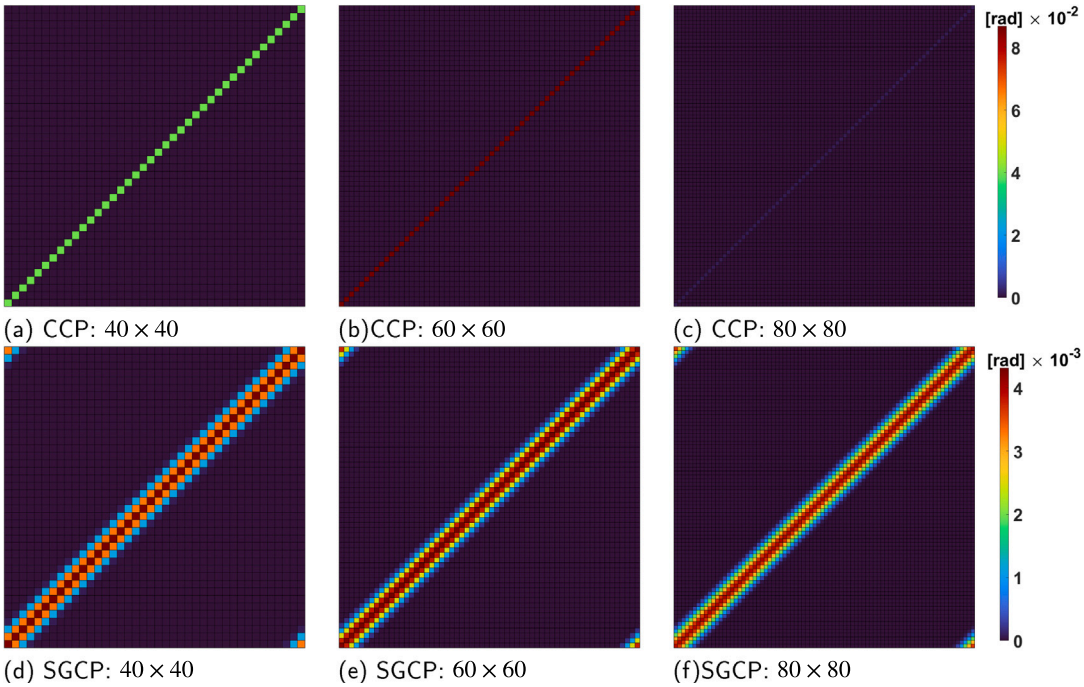

Fig. 6. Single crystal: distribution of the rotation angle (θ).

Three orientations of the single crystal are considered by setting three tensile directions, [123], [001], and [111], in the local coordinate system. In all simulations of this section, the crystal is subjected to tensile loading along the z-direction, including the mean value of the displacement gradient field $\overline{\nabla u}_{zz} = 0.01$ at a relatively low strain rate 10^{-6} s^{-1}, and other components of the Cauchy stress tensor are constrained to zero. Furthermore, the single crystal in the FEM is discretized by the 500 C3D4 elements.[13] In order to allow the localization bands to flow naturally within the crystal due to multiple slip systems, there is no defect in the center, and all material parameters are set to the Table 3 except $\gamma_0 = 0.0125$ and $\triangle\tau = 40$ MPa.

Fig. 8 shows tensile curves for this single crystal with different orientations. Inset (a) of Fig. 8 presents the comparison between the FEM results from the Umat-Abaqus subroutine and the proposed FFT-homogenization method under the same periodic boundary condition and CCP framework. In all cases, perfect agreement is observed in terms of the linear elastic behavior at the initial part of deformation, the dependence of yield stress on the orientation of the crystal, and nonlinear softening behavior. Inset (b) of Fig. 8 illustrates the effect of resolution (number of voxels) on the softening behavior in both the CCP and proposed SGCP (MicroContinuity higher order boundary condition and A = 10^{-4} N) frameworks. In the CCP framework, increasing the number of voxels from 32 × 32 × 32 to 64 × 64 × 64 leads to an increased softening rate after a certain point during deformation, causing the macroscopic tensile curves to suddenly diverge from other curves due to the instability induced by the increased number of

[13] Four-node tetrahedral element.

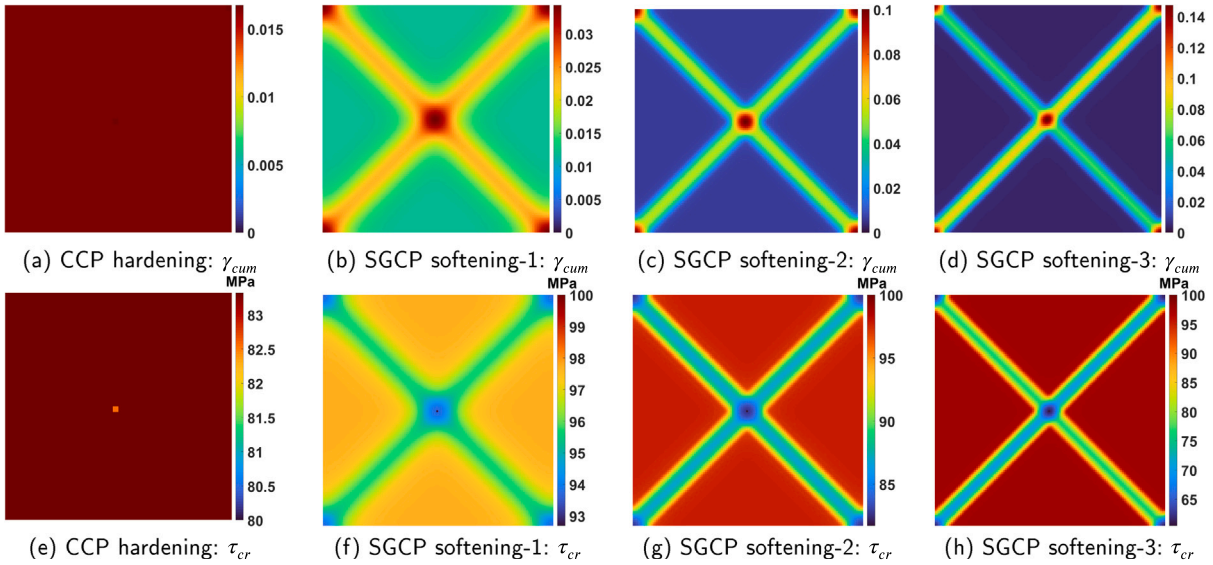

Fig. 7. Distributions of the cumulative shear strain (γ_{cum}) and critical resolved shear stress (τ_{cr}) in a single crystal under tensile loading at the end of deformation ($\overline{\nabla u}_{yy} = 0.01$), displaying the effect of different material parameters.

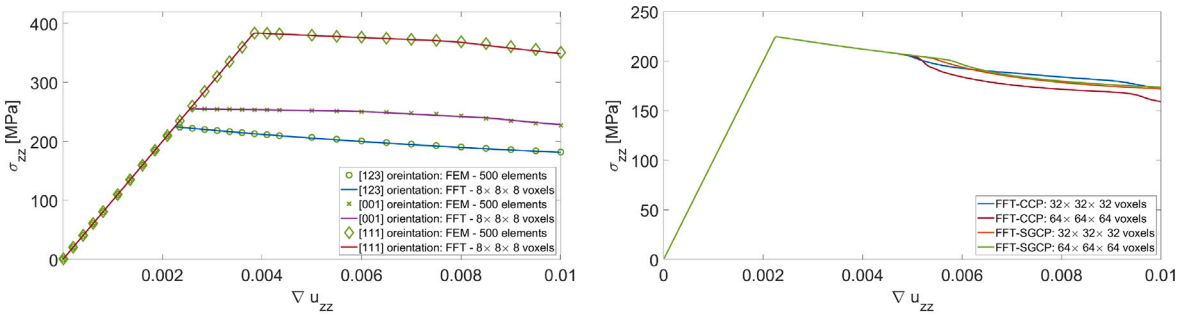

(a) CCP framework: FEM and FFT comparison for different grain orientations

(b) [123] orientation: CCP and SGCP comparison for different grid resolutions

Fig. 8. Three-dimensional single crystal: tensile curves.

voxels. Interestingly, the results of the proposed SGCP framework indicate that the macroscopic tensile curves for these different resolutions almost coincide, demonstrating that the results are voxel-independent in this nonlinear softening behavior.

Fig. 9 exhibits the instability and voxel dependency of the computational results in the CCP framework for the distribution of the total cumulative shear strain at the end of deformation $\overline{\nabla u}_{zz} = 0.01$ from the simulations in Fig. 8 inset (b). For example, by increasing the number of voxels by a factor of two in each Cartesian direction, the localization bands become more concentrated with higher amplitude, and the number of bands increases within the crystal. Furthermore, Fig. 10 presents the distributions from the SGCP framework, which maintains the number, width and amplitude of the bands constant despite the increase in the number of voxels. Additionally, the higher order stresses associated with different slip systems, as described by Eq. (16), are plotted in Fig. 11, showing different distributions for different slip systems. Accordingly, it is concluded that the proposed SGCP model performs correctly in three-dimensional crystalline materials and confirms that the higher order stress is computationally evaluated based on its own slip system and does not affect other slip systems by the proposed flow potential in Eq. (20).

3.5. Polycrystalline aggregate

In this section, the periodic Voronoi tessellation of a polycrystalline aggregate with dimensions of 1 mm × 1 mm is considered. The microstructure is composed of 200 randomly oriented columnar grains[14] (Quey et al., 2011), Fig. 12 . The analysis in this section

[14] Mean grain size $l_p^2 = 1/200$ mm^2.

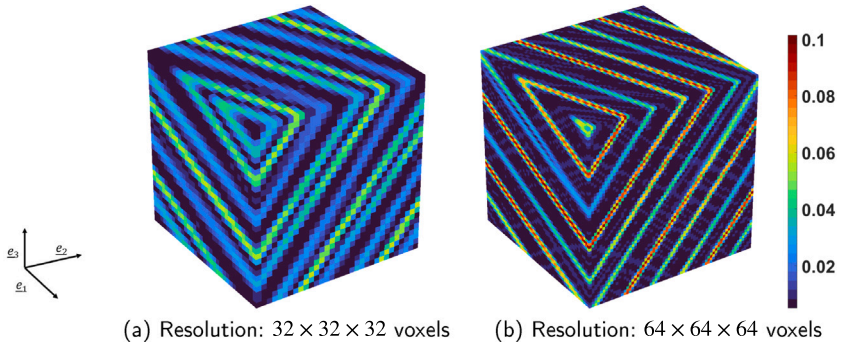

Fig. 9. Three-dimensional single crystal with [123] orientation: distributions of cumulative shear strain, γ_{cum}^{tot}, from the CCP framework at the end of deformation ($\overline{\nabla u}_{zz} = 0.01$) at different resolutions.

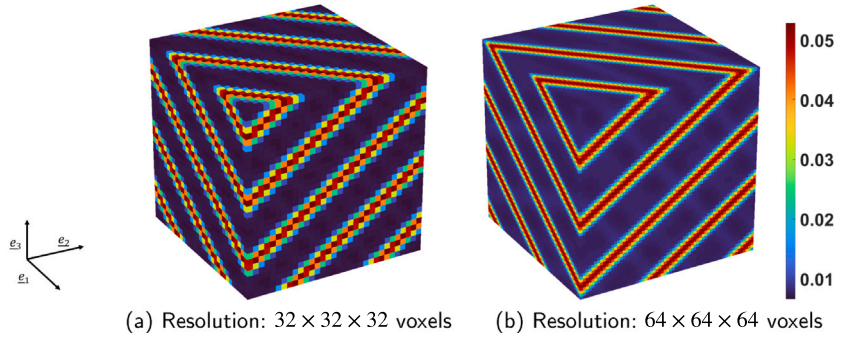

Fig. 10. Three-dimensional single crystal with [123] orientation: distributions of cumulative shear strain, γ_{cum}^{tot}, from the SGCP framework at the end of deformation ($\overline{\nabla u}_{zz} = 0.01$) at different resolutions.

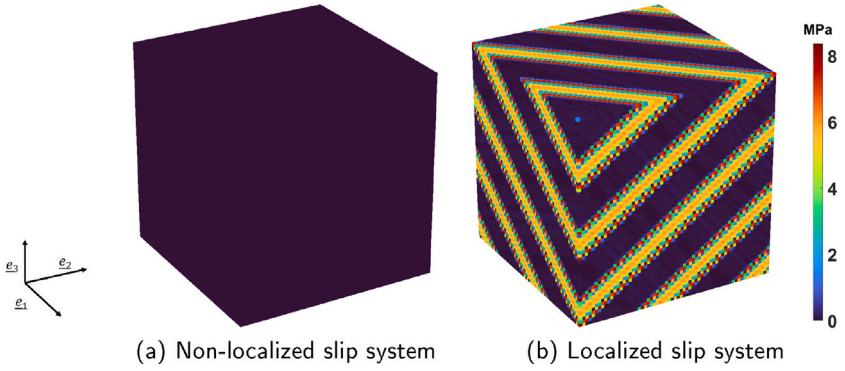

Fig. 11. Three-dimensional single crystal with [123] orientation: distributions of the absolute value of higher order stress, $|S^{\alpha}|$, associated with different slip systems from the SGCP framework at the end of deformation ($\overline{\nabla u}_{zz} = 0.01$).

compares the localization patterns, their regularization, and prediction of size effects using the proposed SGCP model against the CCP framework and experimental observations in a polycrystalline aggregate. At low tensile strains (e.g. 0.01), localization (shear) bands usually initiate and propagate within a single slip system, exhibiting severe plastic deformation in a narrow lamellar region. The corresponding experimental observations often depict these shear bands as parallel lines on the surface of a sample (Di Gioacchino and da Fonseca, 2015; Thomas et al., 2019). In this view, one planar slip system per grain is sufficient to reproduce main localization features observed in experiments[15] at relatively low strain (e.g. 0.01). Using $N_{\alpha} = 1$, two potential perpendicular directions in terms of slip bands and kink bands can be induced in each grain as demonstrated in the single crystal case in the previous section.

[15] Experimental observations confirm that in many grains only one slip system is activated for the applied range of tensile loading used in this study (Di Gioacchino and da Fonseca, 2015).

Table 3
Material properties of polycrystalline aggregate.

E	ν	K	n	τ_0	$\triangle\tau$	γ_0	H
100 GPa	0.3	10 MPa s^{-n}	15	100 MPa	50 MPa	0.05	0 MPa

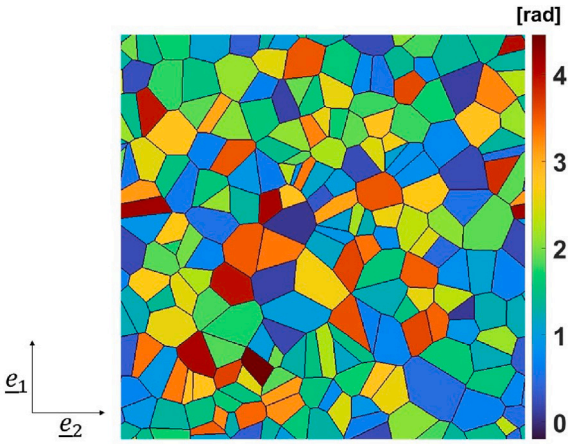

Fig. 12. Geometry of the polycrystalline aggregate composed of 200 grains: different colors correspond to different orientations with respect to the loading direction (absolute value of Euler angle) and black lines are grain boundary voxels. (For interpretation of the references to color in this figure legend, the reader is referred to the web version of this article.)

Planar slip systems are aligned[16] with grain orientations which are assumed random. In all subsequent simulations, the material properties of the constitutive model (Eqs. (21), (22)) remain constant, detailed in Table 3, unless explicitly stated otherwise. The elastic parameters, such as Young's modulus and Poisson's ratio, match those used in single crystalline simulations. The Norton flow exponent and coefficient reflect typical values for the viscoplastic behavior of austenitic stainless steel. Additionally, softening parameters are set based on investigations in single crystal simulations (see Fig. 7): $\gamma_0 = 0.05$ is chosen to expedite localization initiation, and a maximum softening parameter of $\triangle\tau = 50$ MPa is set to increase the softening in the shear bands.[17] Furthermore, the polycrystal is subjected to tensile loading along the y-direction, inducing the mean value of the displacement gradient $\overline{\nabla u}_{yy} = 0.01$, at a relatively low strain rate 10^{-6} s^{-1}, while all other components of the Cauchy stress tensor are constrained to zero.[18]

3.5.1. Regularization of the macroscopic behavior

Initially, the polycrystalline aggregate is analyzed with different grid resolutions to assess the influence of the CCP framework and the impact of higher order boundary conditions from SGCP on the macroscopic behavior. The grid resolutions selected are 40×40, 50×50, and 60×60 voxels per grain, equivalent to a total of 570×570, 710×710, and 850×850 voxels, respectively. Fig. 13 compares the tensile curves calculated with the CCP and SGCP models using different interface conditions. All behaviors exhibit macroscopic hardening up to 1 percent tensile loading ($\overline{\nabla u}_{yy} = 0.01$). The distributions of cumulative shear strain in Figs. 14, 15, 16, and 17 reveal that most parts of the polycrystalline material remain elastic ($\gamma_{cum} = 0$). This is attributed to the fact that the grains, each possessing only one slip system, are randomly oriented. This results in a reduced Schmid factor. Consequently, only a subset of the grains initiates plastic deformation. In addition, due to relatively large amplitude of the softening parameters, such as the maximum softening parameter ($\triangle\tau = 50$ MPa), plastic deformation in those grains is concentrated into the narrow shear bands. Accordingly, the elastic behavior outside of the shear bands macroscopically overcome the microscopic softening within the shear bands, resulting in the observed macroscopic hardening. The SGCP model exhibits significantly higher macroscopic stresses, primarily due to the presence of isotropic hardening term (higher order stress) in the SGCP model. While MicroContinuity and MicroFree cases exhibit approximately similar macroscopic behaviors, the MicroHard condition generates the strongest hardening by preventing the transgranular dislocation movements. Furthermore, when altering the grid resolution of the polycrystalline aggregate, it becomes evident that the CCP framework yields resolution-dependent results. In contrast, the MicroContinuity SGCP model does not exhibit dependence on grid resolution.[19]

[16] By employing the $Z_1X_2Z_3$ type of Bunge convention representation of Euler angles.

[17] Same parameters were used in Marano et al. (2019, 2021) for the irradiated material.

[18] These constraints are subjected to the macroscopic behavior applied at zero frequency in the Fourier (complex) space.

[19] The consistent regularization is also achieved for the SGCP MicroFree model, while grid dependency becomes apparent in the SGCP MicroHard condition. This discrepancy arises from the higher order interface condition on the grain boundary, as described by Eq. (26), which possesses an intrinsic length scale equal to the voxel size.

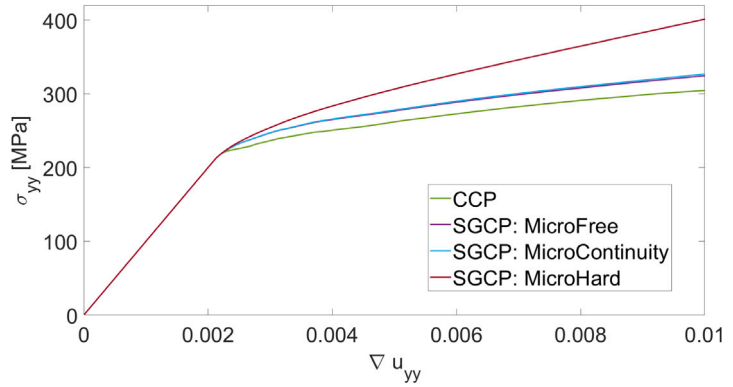

(a) Grid resolution: 50×50 voxels per grain

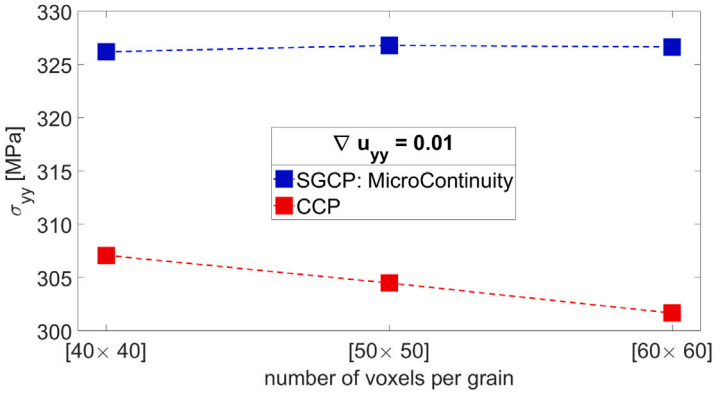

(b) Grid resolution effect at $\overline{\nabla u}_{yy} = 0.01$

Fig. 13. Polycrystalline aggregate: tensile curves for $A = 10^{-3}$ N.

3.5.2. Regularization of the localization bands

The distributions of cumulative shear strain, von-Mises stress, and rotation angle are shown in Figs. 14–17 at final displacement gradient $\overline{\nabla u}_{yy} = 0.01$. The distribution of cumulative shear strain in the polycrystalline simulation illustrated in Fig. 14 exhibits voxel dependency within the CCP framework. Notably, the localization bands have typically the width of one voxel, and their intensity varies with different grid resolutions. Moreover, similar to the CCP results shown in Fig. 4(c), some kink bands tend to disappear at higher grid resolutions.

On the other hand, results in Figs. 15–17 obtained from the SGCP model demonstrate no dependency on grid resolution (objective), consistently maintaining both the width and intensity of localization bands across various higher order boundary conditions when the grid resolution is altered. The localization patterns for MicroFree and MicroContinuity, as shown in Figs. 15 and 16, are generally the same, with slight differences in corresponding intensities. The CCP, SGCP MicroFree, and SGCP MicroContinuity models predict same types of localization bands, as shown in Figs. 14–16(c,e). Bands with finite θ amplitude are identified as kink bands. Upon comparing insets (c) and (e) in Figs. 14–16, it appears that slip and kink bands occur in approximately equal proportions, consistent with the single crystal simulations in Section 3.3. However, the MicroHard condition shown in Fig. 17 displays distinct localization patterns, where the localization bands are predominantly intragranular. The most distinct feature compared to other higher order interface conditions and CCP results is the presence of numerous parallel slip bands within the grains (see Figs. 17(a)). As a result, plastic deformation is more evenly distributed over these bands. Since plastic deformation is not allowed to transmit across the grains, stress concentrates at grain boundaries where the bands meet from both sides, a phenomenon less commonly observed for other conditions.

The capability to regularize the localization bands and control their transmission through grain boundaries by utilizing a single non-local parameter A along with various higher order interface conditions, renders the proposed SGCP model a valuable tool for simulating polycrystalline materials exhibiting softening behavior, such as dislocation channeling in irradiated steels.

3.5.3. Size effect

In the previous section, the results are presented for a fixed aggregate size of 1 mm × 1 mm with a constant non-local parameter of $A = 10^{-3}$ N. In this section, the effect of microstructure size is investigated by keeping the number of grains fixed at 200 and maintaining the same grid resolution of 50 × 50 voxels per grain, as well as using the same material parameters specified in Table 3.

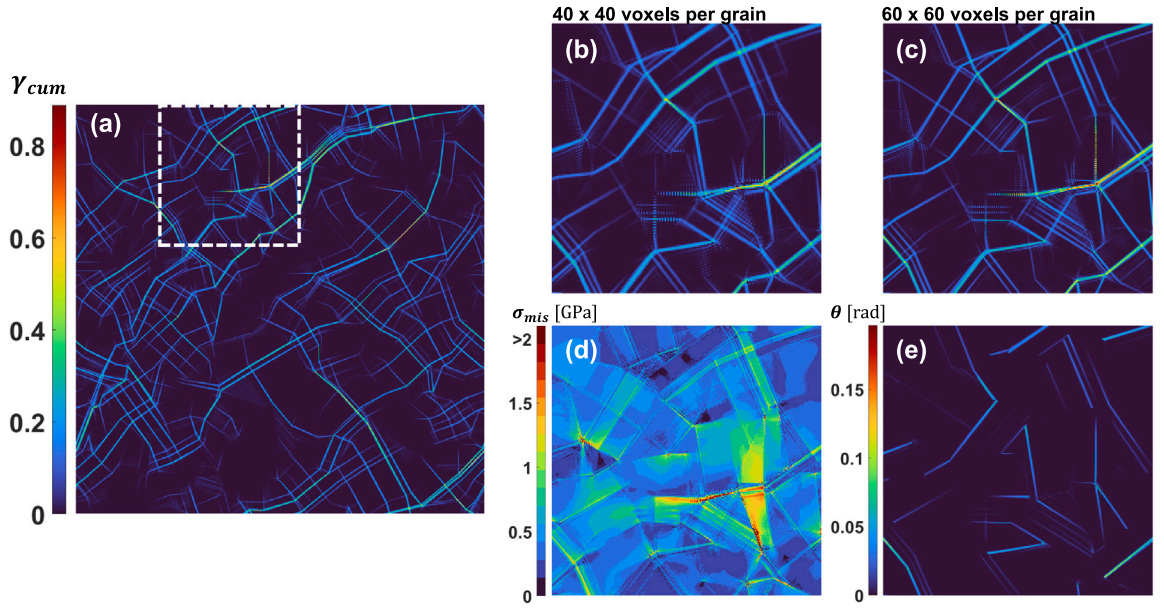

Fig. 14. (a) Distribution of cumulative shear strain (γ_{cum}) in polycrystalline aggregate from the CCP framework using 60 × 60 voxels per grain. Insets (b) and (c) show γ_{cum} at two grid resolutions. Insets (d) and (e) show von-Mises stress and rotation angle at 60 × 60 voxels per grain.

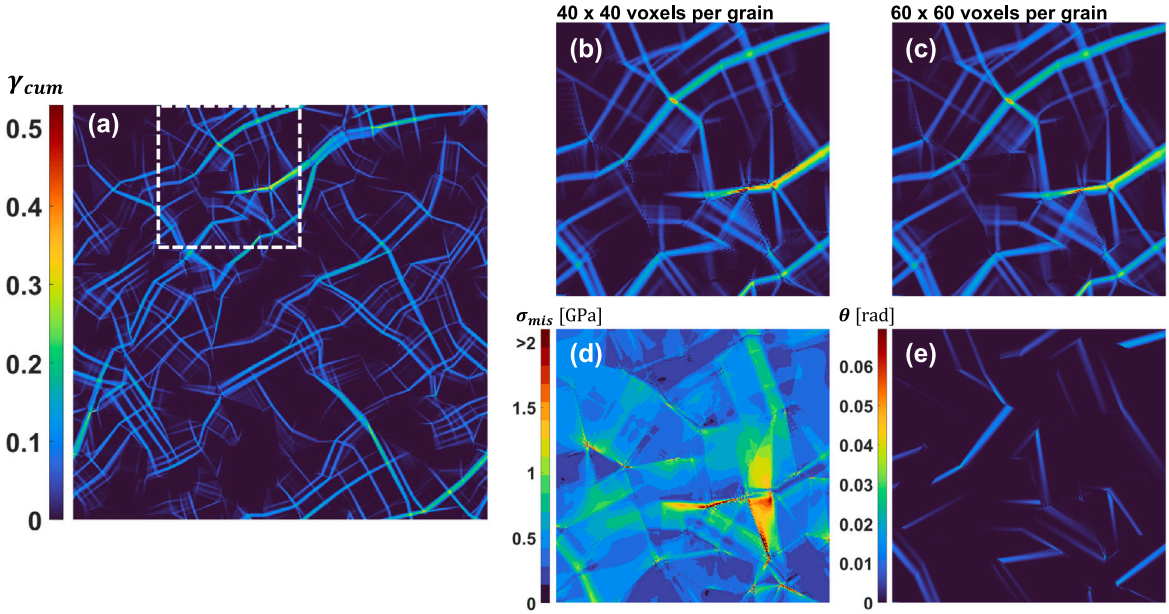

Fig. 15. (a) Distribution of cumulative shear strain (γ_{cum}) in polycrystalline aggregate from the SGCP MicroFree model using 60 × 60 voxels per grain. Insets (b) and (c) show γ_{cum} at two grid resolutions. Insets (d) and (e) show von-Mises stress and rotation angle at 60 × 60 voxels per grain.

The dimensions are varied to capture the macroscopic and microscopic behaviors associated with size effects. Accordingly, three microstructures with dimensions of 1 mm × 1 mm, 0.1 mm × 0.1 mm, and 0.01 mm × 0.01 mm are selected for this analysis. The non-local parameter is adjusted to $A = 10^{-4}$ N for the first two microstructures and $A = 10^{-5}$ N for the smallest microstructure.[20] Higher order interface conditions, including MicroFree and MicroContinuity, are applied at the grain boundaries.

[20] This adjustment is made to avoid overestimating the GND effect, as discussed in Appendix A.

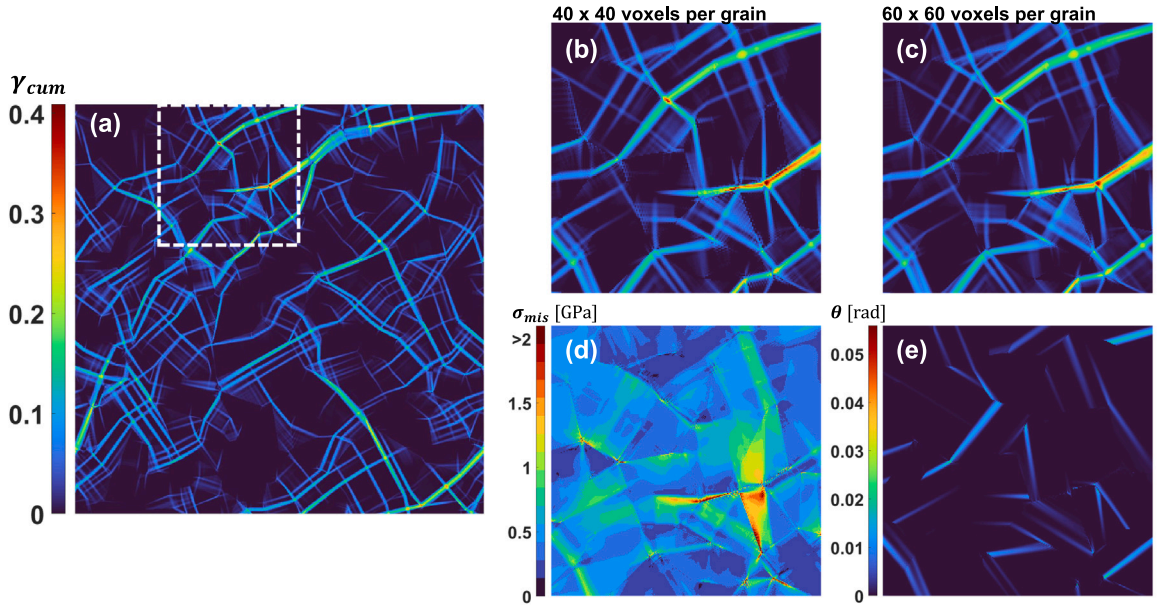

Fig. 16. (a) Distribution of cumulative shear strain (γ_{cum}) in polycrystalline aggregate from the SGCP MicroContinuity model using 60 × 60 voxels per grain. Insets (b) and (c) show γ_{cum} at two grid resolutions. Insets (d) and (e) show von-Mises stress and rotation angle at 60 × 60 voxels per grain.

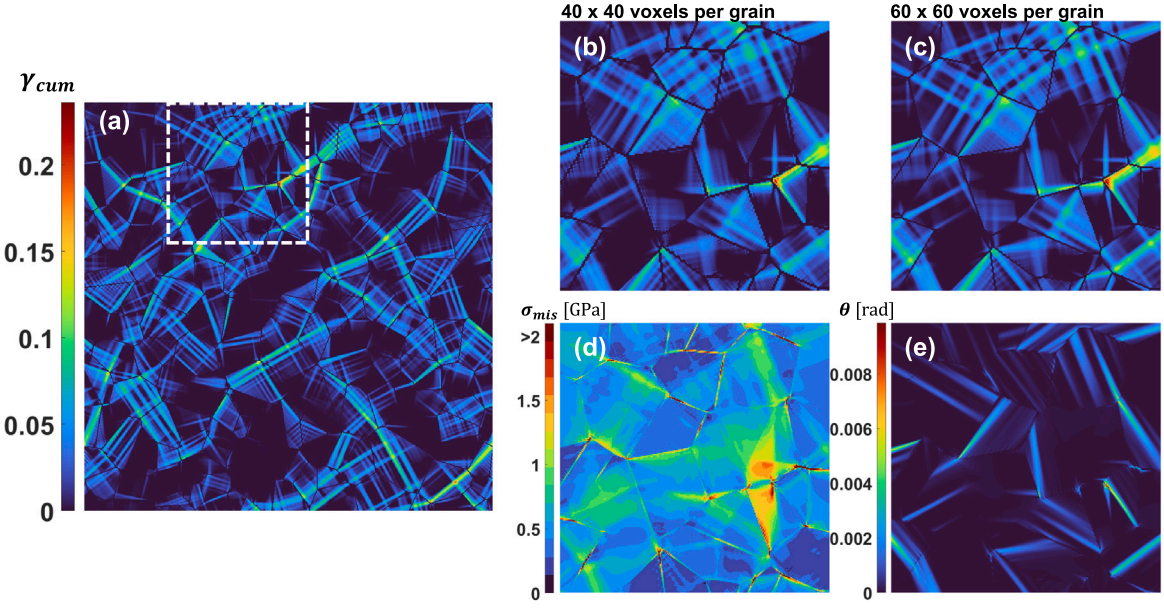

Fig. 17. (a) Distribution of cumulative shear strain (γ_{cum}) in polycrystalline aggregate from the SGCP MicroHard model using 60 × 60 voxels per grain. Insets (b) and (c) show γ_{cum} at two grid resolutions. Insets (d) and (e) show von-Mises stress and rotation angle at 60 × 60 voxels per grain.

Fig. 18 displays the tensile curves for all microstructures under the applied higher order interface conditions at the grain boundaries. In general, smaller microstructures demonstrate higher macroscopic stress during plastic deformation. This is in agreement with the fact that smaller grains possess larger total area of grain boundaries per unit volume, leading to a higher density of obstacles for dislocation (localization band) glide. Additionally, slight differences between the MicroFree and MicroContinuity conditions are observed in the microstructures with dimensions of 0.1 mm × 0.1 mm and 0.01 mm × 0.01 mm. The MicroContinuity condition in these microstructures results in approximately 10 percent higher macroscopic stress at the end of deformation ($\overline{\nabla u}_{yy}$ = 0.01).

Fig. 19 illustrates the distributions of cumulative shear strain and von-Mises stress in the microstructures with the dimensions of 0.01 mm × 0.01 mm and 1 mm × 1 mm under the MicroFree condition. In the smaller microstructure, the localization bands

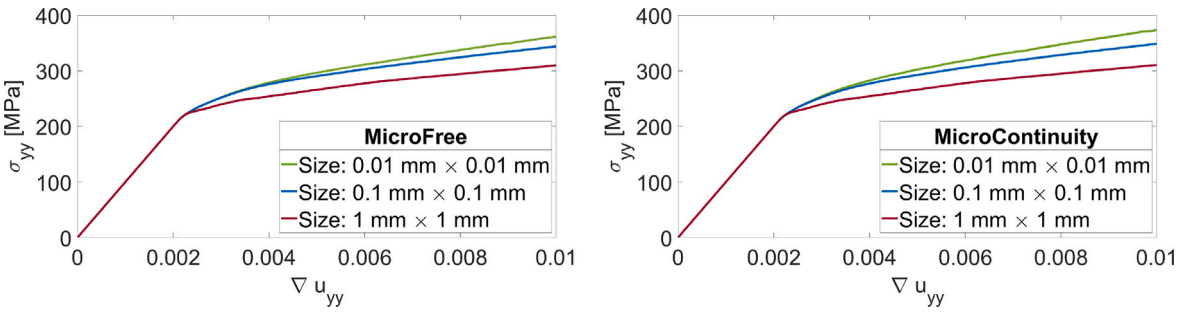

Fig. 18. Aggregate size effect on tensile behavior.

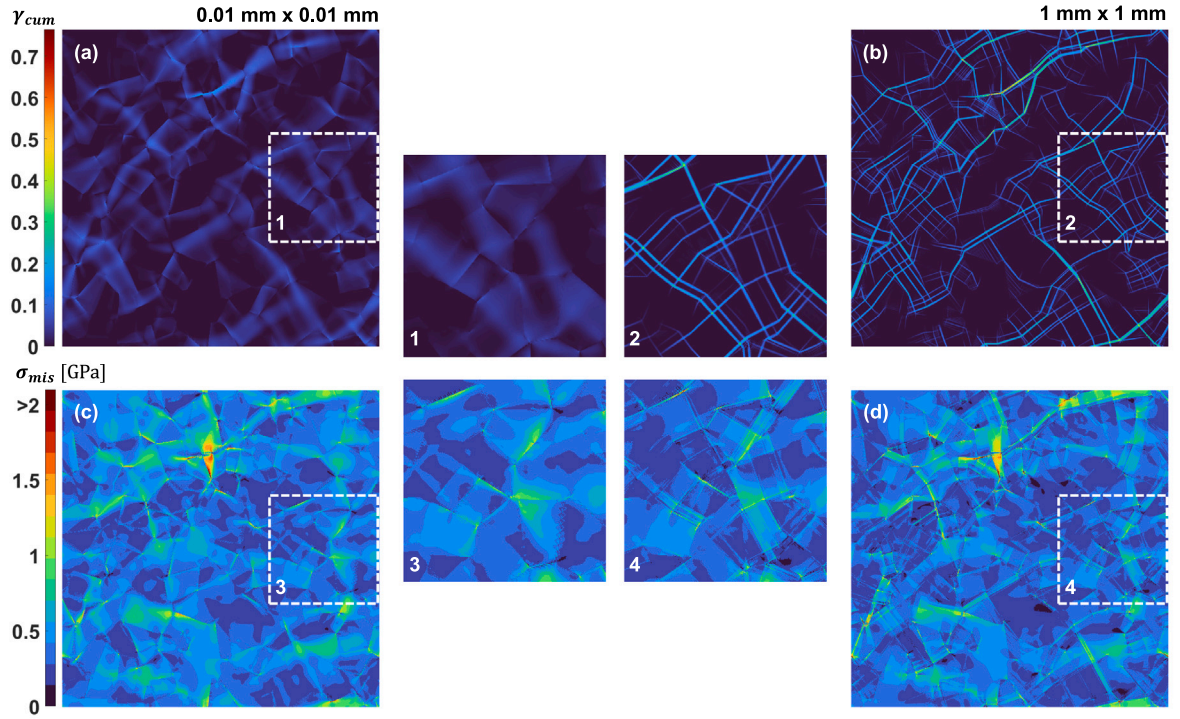

Fig. 19. Size effect in polycrystalline aggregate: SGCP MicroFree framework. Distributions of (a) cumulative shear strain in smaller microstructure (b) cumulative shear strain in larger microstructure (c) von-Mises stress in smaller microstructure (d) von-Mises stress in larger microstructure.

have a relatively wider width (almost homogeneous) and contain a lower amount of cumulative shear strain compared to the larger microstructure. Consequently, the von-Mises stresses are typically less localized in the smaller microstructure, showing also relatively fewer concentration spots near the grain boundaries. Practically identical patterns are observed under the MicroContinuity condition compared to the MicroFree condition, albeit with slight differences near grain boundaries (not shown).

3.6. Comparison with experimental results

In this section, the results from the proposed SGCP model are compared and discussed in relation to experimental testing on both unirradiated and irradiated materials. One particular experimental study is considered, which involves a Zircaloy specimen (Thomas et al., 2019), nominally Zr-1.5Sn-0.2Fe-0.1Cr, subjected to less than 2 percent tensile loading in both unirradiated and irradiated planar polycrystals. The purpose of the experiment was to observe shear bands using high-resolution digital image correlation (HRDIC) and electron backscatter diffraction (EBSD). In addition to novel experimental techniques, instruments, and image processing used in that study, important mechanical details relevant for numerical comparisons are mentioned here. The Zircaloy polycrystal with the approximate grain size of 10^{-5} m was irradiated using proton acceleration resulting in final irradiation damage ranging between 0.09 to 0.13 dpa (displacements per atom). The uniaxial tensile test was conducted at room temperature with a strain amplitude of 2 percent and an initial strain rate of 1.6×10^{-4} s^{-1}.

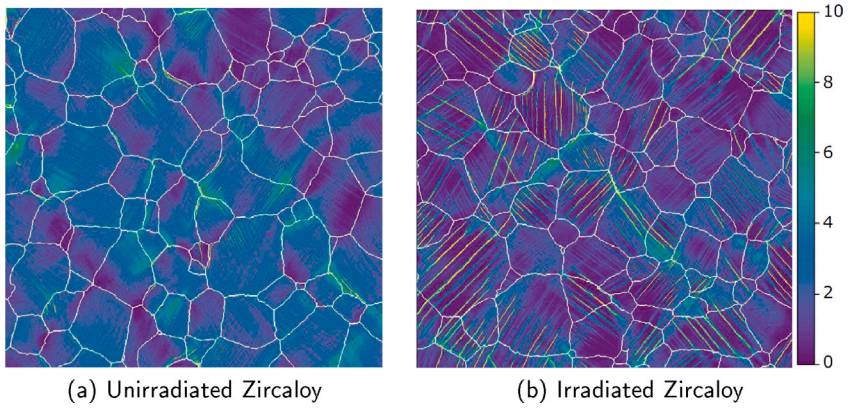

Fig. 20. Measured distributions of (effective) shear strain in percent (a) unirradiated and (b) irradiated Zircaloy polycrystal after 2 percent tensile loading. White lines correspond to grain boundaries.
Source: Taken from Thomas et al. (2019).

Fig. 20 illustrates the distribution of shear bands in unirradiated and irradiated Zircaloy polycrystalline materials, based on shear strain parameters introduced in the experimental study as representative of local deformation[21] obtained through HRDIC post-processing. Insets (a) and (b) demonstrate an impact of irradiation during tensile testing on the heterogeneous distribution of deformation. While shear bands are closely spaced in unirradiated Zircaloy material, strain localization in the irradiated Zircaloy is noticeably different, featuring distinct bands with higher effective strain amplitudes and almost zero deformation outside the bands. Additionally, deformation in the unirradiated Zircaloy polycrystalline material is concentrated near the grain boundaries; however, in the irradiated material, the highest deformation is predominantly localized within shear bands near the grain centers.

To qualitatively compare the localization pattern with this experimental study, simulations are performed on the Voronoi tessellation model shown in Fig. 12. The model dimensions are set to 1 mm × 1 mm, with each grain size approximately 10^{-5} m. These simulations, conducted under tensile loading with an amplitude of 1 percent, correspond to both unirradiated and irradiated states. To emphasize that the material parameters are chosen based on representative characteristics rather than strictly through a calibration procedure, the resulting material behaviors are labeled as "unirradiated-like" and "irradiated-like". Experimental observations from Onimus et al. (2006) on the macroscopic behaviors of irradiated and unirradiated Zircaloy under mechanical loading indicate that the unirradiated specimen exhibits hardening behavior, while softening behavior is observed under irradiated conditions. Consequently, for the unirradiated state, the initial critical resolved shear stress (yield stress) is set 20 percent lower than that of the irradiated state, with $\tau_0 = 80$ MPa. During the plastic deformation phase, a hardening modulus of $H = 500$ MPa is applied, as described in Eq. (22), with no exponential softening ($\Delta\tau = 0$ MPa). Furthermore, to capture the softening behavior in the irradiated state,[22] the exponential term in Eq. (22) is established with $\Delta\tau = 50$ MPa and $\gamma_0 = 0.05$. In the context of the IASCC mechanism, the grain boundary is recognized as playing a crucial role in the transmission of localization bands (McMurtrey et al., 2011). Particularly in reactor environments, such as pressurized water reactors, the diffusion and penetration of hydrogen and oxygen isotopes at the grain boundary can be several orders of magnitude higher than within the grains (Laghoutaris et al., 2008). These isotopes contribute to the grain boundary becoming brittle and thicker, which, within the IASCC mechanism, is interpreted as an inability of the grain boundary to accommodate and transmit localized plastic deformation, leading to high stresses and potential microcrack initiation. As a result, the application of higher order interface conditions, such as the MicroHard condition, allows for a qualitative consideration of the IASCC mechanism at the grain boundary. Accordingly, numerical simulations for the irradiated state are carried out using the SGCP framework with the MicroHard higher order interface condition applied to grain boundaries, and simulations for the unirradiated state are conducted using both the CCP ($A = 0$ N) and SGCP frameworks. In both unirradiated and irradiated states in SGCP framework, the non-local parameter is set to the amplitude of $A = 10^{-4}$ N.

Fig. 21 depicts the macroscopic behavior of unirradiated-like in both CCP and SGCP frameworks and irradiated-like in SGCP framework under tensile loading. In addition to (imposed) increased yield stress, the irradiated-like aggregate exhibits smaller macroscopic hardening, which results from local exponential softening behavior. Overall, the numerical results confirm typical macroscopic effects of irradiation in polycrystalline aggregate (Pokor et al., 2004; Onimus et al., 2006). Furthermore, the macroscopic behavior of the unirradiated-like state shows almost no difference between the CCP and SGCP frameworks. As shown in Fig. 7, insets (a) and (e), for a single crystal, the hardening behavior does not result in the formation of localization bands. Instead, a homogeneous deformation is observed, leading to a gradient of the cumulative shear strain that is approximately negligible, rendering the higher order stress, Eq. (16), inactive in the shear flow rule, Eq. (21), due to the higher amplitude of the critical

[21] This effective shear strain parameter is not equal to the cumulative shear strain (γ_{cum}) but has the same qualitative meaning.
[22] The remaining parameters not discussed here for the irradiated and unirradiated states are consistent with those provided in Table 3.

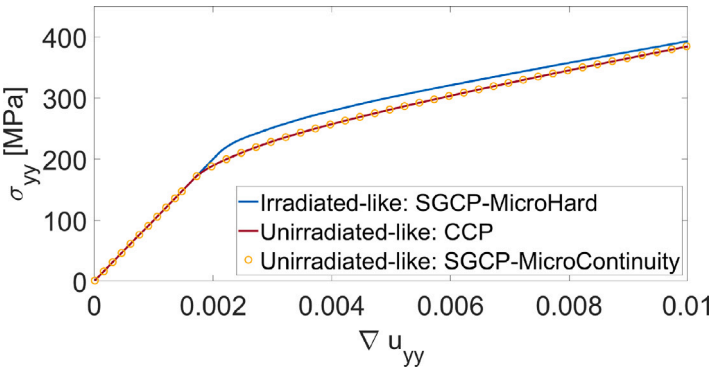

Fig. 21. Calculated tensile curves of the irradiated-like and unirradiated-like polycrystalline material.

resolved shear stress, Eq. (22), in the hardening behavior ($S \ll \tau_{cr}$). As a result, the outcomes from the CCP and SGCP frameworks are nearly identical in the unirradiated state.

Fig. 22 illustrates the microscopic distributions of cumulative shear strain and von-Mises stress at the end of deformation for two polycrystalline aggregates ($\overline{\nabla u}_{yy} = 0.01$). In both unirradiated-like and irradiated-like states, heterogeneous distributions of plastic deformation are observed. In the unirradiated state, as depicted in inset (a) of Fig. 22 and consistent with aforementioned experimental study, shear bands are closely spaced, with strain primarily localized near the grain boundaries. Additionally, in inset (b) of Fig. 22, the shear band distributions differ significantly in the irradiated state, exhibiting highly localized plastic deformation within evenly spaced bundles of parallel shear bands, whereas the space between bands experiences zero plastic deformation. Moreover, some grains display two perpendicular bundles of shear bands in terms of slip and kink bands which are predominantly localized at the grain centers, with reduced intensity toward the grain boundaries. Most of these effects were also observed in the experimental study. The main qualitative difference is the absence of secondary localization bands (due to $N_\alpha = 1$), which, however, are induced in few of the Zircaloy grains (Fig. 20 inset (b)).

In insets (c) and (d) of Fig. 22, the distribution of von-Mises stress is visualized for the unirradiated-like and irradiated-like states of the polycrystalline material. In the unirradiated state, depicted in inset (c) of Fig. 22, the von-Mises stress is distributed more homogeneously across the grains, with some concentration regions close to grain boundaries. Conversely, in the irradiated state, shown in inset (d) of Fig. 22, the von-Mises stress is strongly concentrated in regions where the shear bands intersect the grain boundaries. Such stress concentration spots are potentially risky for the formation of micro cracks in real materials. Indeed, this confirms to be the similar case in IASCC in irradiated austenitic stainless steel under light water reactor conditions (Jiao and Was, 2010). Experimental observations on irradiated materials highlight interactions between shear bands (or clear channels) and grain boundaries (Hesterberg et al., 2019; Howard et al., 2019; Johnson et al., 2019). These interactions lead to dislocation pile-up at grain boundaries, resulting in high stress concentrations and crack initiation. In austenitic stainless steels, clear channels running parallel to grain boundaries, particularly in proximity to triple junctions, have been found to enhance stress states and initiate cracks, [Figure 15 of Hesterberg et al. (2019)]. Similarly, Howard et al. (2019) conducted micro-tensile tests on irradiated stainless steel, observing clear channels on grain boundaries contributing to high stress concentrations and the presence of both transgranular and intergranular bands on fracture surfaces, [Figure 13 of Howard et al. (2019)]. Additionally, Johnson et al. (2019) noted that the region between two clear channels interacting with grain boundaries is prone to crack initiation under tensile loading, [Figure 6 of Johnson et al. (2019)]. In this view, the microscopic results in Fig. 22 qualitatively agree with experimental observations in (un)irradiated structural materials.

To conclude, the proposed SGCP model, complemented by the MicroHard higher order interface conditions on grain boundaries, appears to be a suitable computational tool for predicting strain localization patterns and stress concentrations at grain boundaries in irradiated material under IASCC mechanism.

4. Conclusions

This study proposed a new SGCP model based on cumulative shear strain, referred to as strict MicroSlip, to study the strain localization phenomena in polycrystalline materials. The primary objectives of this study were twofold: firstly, to address the dependency of results on grid resolution in classical framework, and secondly, to regularize both the macroscopic behavior and local evolution of strain localization patterns accounting for the aggregate (or grain) size effects. To achieve these goals, thermodynamically consistent constitutive equations for SGCP model were derived. Subsequently, analytical solutions corresponding to linear hardening, perfect plasticity, and linear softening behaviors were developed.

The proposed SGCP model was implemented within the fixed-point algorithm of the FFT-homogenization method. To enhance the numerical accuracy, various techniques were employed, including the modified Green operator based on the rotated scheme, alternate $2-\delta$ Anderson acceleration method, arc-length method for mixed control of macroscopic stress and displacement gradient, and a 21-finite difference scheme for evaluating the higher order stresses.

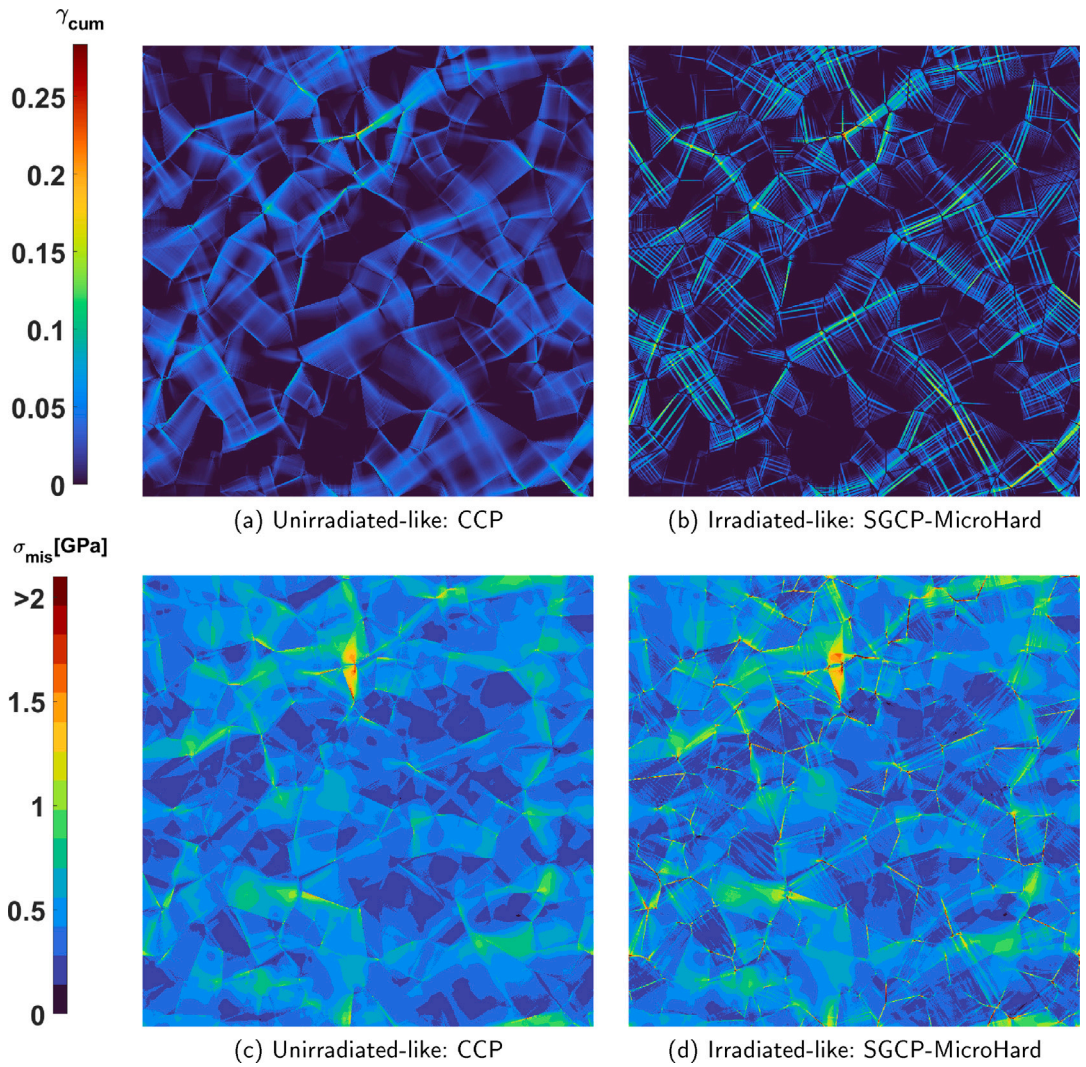

Fig. 22. Calculated distributions of cumulative shear strain and von-Mises stress at the end of deformation $\overline{\nabla u}_{yy} = 0.01$ in the unirradiated-like and irradiated-like polycrystalline material.

The implementation of the SGCP model in the proposed fixed-point algorithm was successfully validated against the analytical solutions. The model was then used to reproduce localization bands in single crystal and polycrystal simulations. While in the CCP framework, the width of localization bands was typically constrained to one voxel size, the results from SGCP remained grid independent, in terms of amplitude and width for both slip and kink bands. Furthermore, the model was applied to simulate polycrystalline aggregates under three higher order boundary conditions (MicroFree, MicroContinuity, MicroHard) on grain boundaries, resulting in regularization of the localization patterns. Under MicroFree and MicroContinuity conditions, intragranular and transgranular bands were observed, whereas in MicroHard conditions, all the bands were intragranular, with substantial stress concentrations emerging at grain boundaries. The proposed SGCP model was also shown to exhibit the (grain) size effects. When varying the size of a polycrystalline aggregate, different responses were obtained for a fixed non-local parameter. Smaller grains provided relatively wider localization bands and stiffer macroscopic responses compared to the larger grains. Comparing with existing experimental results, the proposed SGCP model, complemented by the MicroHard higher order interface conditions on grain boundaries, appears to be a suitable computational tool for predicting strain localization patterns and stress concentrations at grain boundaries in irradiated materials.

Perspectives for future work include the integration of the proposed SGCP model with a MicroCurl model, and the implementation of composite voxels to improve the grid independence of higher order boundary conditions (MicroFree and MicroHard).

CRediT authorship contribution statement

Amirhossein Lame Jouybari: Writing – review & editing, Writing – original draft, Visualization, Validation, Software, Methodology, Investigation, Data curation, Conceptualization. **Samir El Shawish:** Writing – original draft, Supervision, Investigation. **Leon Cizelj:** Writing – review & editing, Supervision, Investigation.

Declaration of competing interest

The authors declare that they have no known competing financial interests or personal relationships that could have appeared to influence the work reported in this paper.

Acknowledgments

The authors gratefully acknowledge the financial support provided by Slovenian Research and Innovation Agency, Slovenia (grants P2-0026 and young researcher Amirhossein Lame Jouybari).

Appendix A. Physical interpretation of higher order stresses and correlation with the Nye's tensor

In a three-dimensional single crystal within a Cartesian coordinate system, consider a slip system characterized by the slip direction $\underline{s} = \underline{e}_1$ and the normal to the slip plane $\underline{m} = \underline{e}_2$. According to Arsenlis and Parks (1999), the edge dislocation density ($\rho_{\vdash}$) and screw dislocation density ($\rho_{\odot}$) within the slip plane can be directly determined from the gradient of the shear strain and the slip direction.

$$\rho_{\vdash} = -\underline{e}_1.\nabla\gamma = -\frac{\partial\gamma}{\partial x_1} \tag{A.1}$$

$$\rho_{\odot} = \left(\underline{e}_1 \times \underline{e}_2\right).\nabla\gamma = \frac{\partial\gamma}{\partial x_3} \tag{A.2}$$

The corresponding higher order stresses, given by Eqs. (15), (16), are projected onto the slip plane, and the yield function for perfect plasticity behavior ($\tau_{cr} = \tau_0$) are recalled here. In this analysis, the slip direction and the normal to the slip plane align with the positive directions of the Cartesian coordinate system, and a single active slip system is considered for the crystal, resulting in $\gamma_{cum} = \gamma$. Additionally, the partial derivatives in the higher order stress can be expressed in terms of the edge and screw dislocation densities, as described by Eqs. (A.1), (A.2).

$$M = A\left(\frac{\partial\gamma_{cum}}{\partial x_1}\underline{e}_1 + \frac{\partial\gamma_{cum}}{\partial x_3}\underline{e}_3\right) = A\left(-\rho_{\vdash}\underline{e}_1 + \rho_{\odot}\underline{e}_3\right) \tag{A.3}$$

$$S = A\left(\frac{\partial^2\gamma_{cum}}{\partial x_1^2} + \frac{\partial^2\gamma_{cum}}{\partial x_3^2}\right) = A\left(-\frac{\partial\rho_{\vdash}}{\partial x_1} + \frac{\partial\rho_{\odot}}{\partial x_3}\right) \tag{A.4}$$

$$f = |\tau| - \tau_0 + S \tag{A.5}$$

Fig. A.1 illustrates the dislocation pile-up mechanism in the slip plane. The figure demonstrates that the partial derivatives of the edge and screw dislocation densities consistently have opposite signs within the loop, $\text{sign}(\frac{\partial\rho_{\vdash}}{\partial x_1}) = -\text{sign}(\frac{\partial\rho_{\odot}}{\partial x_3})$, and therefore do not cancel out in the dislocation pile-up mechanism. Consequently, higher order stress is always present in the dislocation pile-up ($S \neq 0$). This leads to the conclusion that the higher order stresses S and M are arising from the energy stored in the dislocation pile-ups, which resist the glide of dislocations.

To characterize the non-local parameter A, a dimensionless coordinate system is introduced in the slip plane, defined by $x_1' = \frac{x_1}{l_p}$ and $x_3' = \frac{x_3}{l_p}$, where l_p represents the characteristic length scale. Using this dimensionless coordinate system, the higher order stress and yield function in Eqs. (A.4), (A.5) are transformed into the following equations.

$$S = \frac{A}{l_p^2}\left(\frac{\partial^2\gamma_{cum}}{\partial x_1'^2} + \frac{\partial^2\gamma_{cum}}{\partial x_3'^2}\right) \tag{A.6}$$

$$f = \tau - \tau_0 + \frac{A}{l_p^2}\left(\frac{\partial^2\gamma_{cum}}{\partial x_1'^2} + \frac{\partial^2\gamma_{cum}}{\partial x_3'^2}\right) \tag{A.7}$$

Once plastic deformation begins, the yield function equals zero ($f = 0$).

$$\tau = \tau_0 - \frac{A}{l_p^2}\left(\frac{\partial^2\gamma_{cum}}{\partial x_1'^2} + \frac{\partial^2\gamma_{cum}}{\partial x_3'^2}\right) \tag{A.8}$$

Therefore, in the perfect plasticity behavior, higher order stress can be interpreted as a variation in yield strength induced by Geometrically Necessary Dislocations (GNDs). The influence of GNDs varies depending on the ratio of A/l_p^2 relative to the initial yield stress (τ_0). Accordingly, three possible scenarios are considered: first, when $A/l_p^2 \ll \tau_0$, the effect of higher order stress on yield strength is negligible ($S \ll \tau_0 \Rightarrow f \cong \tau - \tau_0$). Second, when $A/l_p^2 \cong \tau_0$, the GNDs or higher order stress properly influence the

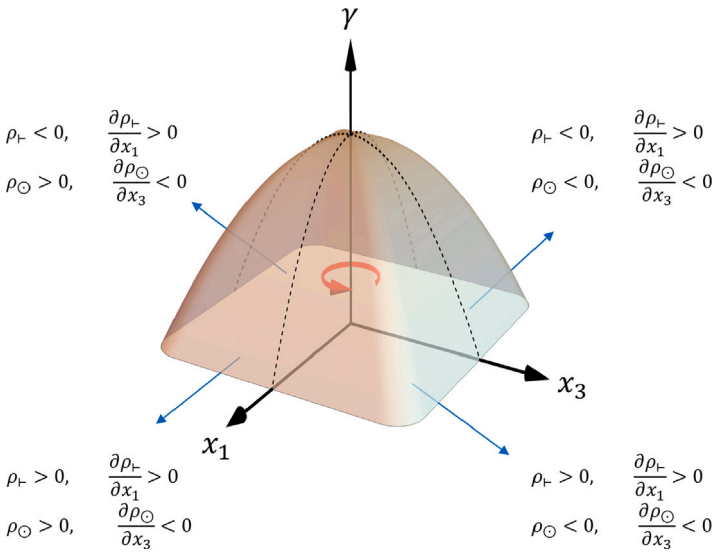

Fig. A.1. Schematic mechanism of dislocation pile-up by the evolution of screw and edge dislocation density in the slip plane. Dislocation lines orientation is indicated by the red signed loop.

yield strength of the crystal ($S \cong \tau_0 \Rightarrow f = \tau - \tau_0 + S$). Third, when $A/l_p^2 \gg \tau_0$, the effect of GNDs is overestimated ($S \gg \tau_0$). It is concluded here that the non-local parameter is proportional to $A \propto \tau_0 l_p^2$.

Furthermore, to establish a relationship between the higher order stress and Nye's tensor, a definition of Nye's tensor based on the edge and screw dislocation densities is recalled here (Gurtin, 2002) for the specific single crystal discussed at the beginning of this section and in the small deformation framework (Marano et al., 2021).

$$\underset{\sim}{\alpha} = \rho_{\odot} \underline{e}_1 \otimes \underline{e}_1 + \rho_{\vdash} \underline{e}_1 \otimes \underline{e}_3 = -\nabla \times \left((\nabla \underline{u})^p \right) \tag{A.9}$$

Following the studies that consider the Nye's tensor as a strain gradient variable (Marano et al., 2021; Lebensohn and Needleman, 2016), the back-stress term, χ, in those studies is calculated here.

$$\chi = -A \nabla \times \left(-\underset{\sim}{\alpha} \right) : \underline{s} \otimes \underline{m} = A \left(\frac{\partial \rho_{\vdash}}{\partial x_1} - \frac{\partial \rho_{\odot}}{\partial x_3} \right) \tag{A.10}$$

It is thus concluded that the back-stress in the Nye's tensor SGCP model is equal in magnitude but opposite in sign to the higher order stress in the proposed SGCP model ($\chi = -S$), due to their differing evolution in the shear flow rule.

Appendix B. Dislocation based crystal plasticity model accounting for clear channel mechanism

In this section, the material parameters within the proposed crystal plasticity model are calibrated based on the dislocation-based crystal plasticity method proposed for irradiated Zircaloy (Onimus and Béchade, 2009) to reproduce clear channels. The irradiation induces hardening defects in the microstructure in form of loops with a diameter of d, which act as obstacles to dislocation glide. According to the dispersed barrier hardening model, this results in an evolution to the critical resolved shear stress in the dislocation-based crystal plasticity model ($\delta\tau_{cr} = \tau_{cr}^{Ir} - \tau_{cr}^{UnIr}$).

$$\delta\tau_{cr}^{\alpha} = \beta \mu b \sqrt{N d} \tag{B.1}$$

where b, β, N, and μ are respectively the Burgers vector, the proportionality factor of the obstacle strength, the number of hardening defects, and the shear modulus. Accordingly, the total critical resolved shear stress is expressed by summing the initial yield stress (τ_{cr}^0) and introducing the density of hardening defects ($\rho_L = N/d$).

$$\tau_{cr}^{\alpha} = \tau_{cr}^0 + \delta\tau_{cr}^{\alpha} = \tau_{cr}^0 + \beta \mu b \sqrt{\rho_L} \tag{B.2}$$

The initiation of dislocation glide within the plastic region of deformation interacts with pre-existing defects, leading to the softening of the material by clearing these defects within the channel. This sweeping mechanism can be modeled by assuming that all defects, are distributed at a distance of $H/2$ from the dislocation plane, interact with dynamic dislocations characterized by a density ρ and velocity $\bar{v}$ over specific time. Consequently, the number of defects removed from the channels is given by $N H \rho \bar{v} dt$, and using the Orowan equation leads to expression of the plastic shear strain rate $\dot{\gamma} = \rho b \bar{v}$. Therefore, the defect density can be described by the following expression, assuming single slip activation during the formation of a dislocation channel.

$$\frac{d\rho_L}{dt} = -\frac{H}{b}\rho_L|\dot{\gamma}^\alpha| \tag{B.3}$$

Consequently, the solution is obtained through time integration and solving differential equation.

$$\rho_L = \rho_{L0} exp(-\frac{H}{b}|\gamma|) \tag{B.4}$$

By substituting the expression for ρ_L into Eq. (B.2), the critical resolved shear stress for the clear channel is obtained.

$$\tau^\alpha_{cr} = \tau^0_{cr} + \beta\mu b\sqrt{\rho_{L0}} exp(-\frac{H}{2b}|\gamma|) \tag{B.5}$$

Finally, by comparing Eq. (B.5) with Eq. (22) under irradiation conditions (no hardening modulus or $H^\alpha = 0$), the material parameters in the proposed crystal plasticity model are calibrated with respect to the dislocation-based model.

$$\gamma_0 = \frac{2b}{H} \tag{B.6}$$

$$\Delta\tau = \beta\mu b \tag{B.7}$$

$$\tau_0 = \tau^0_{cr} + \beta\mu b \tag{B.8}$$

Appendix C. Anderson acceleration

This FFT-homogenization algorithm employs a specific type of Anderson acceleration known as the alternate $2-\delta$ method, which has been reported to provide superior performance compared to other types in the literature (Ramière and Helfer, 2015). This particular Anderson acceleration method is briefly outlined here. Within this method, a vector field $\underline{y}$ with dimension $\mathbb{R}^N$ evolves by the following nonlinear fixed-point equation,[23]

$$\underline{y} = G(\underline{y}), \quad \underline{y} \in \mathbb{R}^N, \quad G : \mathbb{R}^N \to \mathbb{R}^N \tag{C.1}$$

where due to the fixed point iterations, the vector field at new iteration is evaluated by the field at previous iteration,

$$\underline{y}_{n+1} = G(\underline{y}_n) \tag{C.2}$$

In this equation, $\underline{y}_{n+1}$ corresponds to the solution of the vector field at the new iteration. This type of Anderson acceleration is activated every three iterations to extrapolate the new accurate solution,

$$\underline{y}_{n+1} = \underline{y}_n - \lambda^1_n\left[\underline{y}_n - \underline{y}_{n-1}\right] - \lambda^2_n\left[\underline{y}_n - \underline{y}_{n-1}\right] \tag{C.3}$$

where the expressions of the two scalar parameters λ^1_n and λ^2_n are solved by minimizing the following constraint,

$$\delta\underline{y}_n = \underline{y}_n - \underline{y}_{n-1} - \lambda^1_n\left[\underline{y}_n - 2\underline{y}_{n-1} + \underline{y}_{n-2}\right] - \lambda^2_n\left[\underline{y}_{n-1} - 2\underline{y}_{n-2} + \underline{y}_{n-3}\right] \tag{C.4}$$

Appendix D. Finite difference scheme

The fast Fourier transform ($\mathcal{FFT}$) and inverse fast Fourier transform ($\mathcal{IFFT}$) of a scalar field g are defined for the periodic microstructure, discretized into $N_{\text{tot}} = N_1 \times N_2 \times N_3$ voxels, as follows (in discrete Fourier transform notations):

$$\hat{g}(\xi_1,\xi_2,\xi_3) = \mathcal{FFT}\left(g\right) = \frac{1}{N_{tot}}\sum_{x_1=0}^{N_1-1}\sum_{x_2=0}^{N_2-1}\sum_{x_3=0}^{N_3-1} g(x_1,x_2,x_3)\exp\left(-2\pi\mathrm{j}\left(\frac{\xi_1 x_1}{N_1} + \frac{\xi_2 x_2}{N_2} + \frac{\xi_3 x_3}{N_3}\right)\right) \tag{D.1}$$

$$g(x_1,x_2,x_3) = \mathcal{IFFT}\left(\hat{g}\right) = \sum_{\xi_1=0}^{N_1-1}\sum_{\xi_2=0}^{N_2-1}\sum_{\xi_3=0}^{N_3-1} \hat{g}(\xi_1,\xi_2,\xi_3)\exp\left(2\pi\mathrm{j}\left(\frac{\xi_1 x_1}{N_1} + \frac{\xi_2 x_2}{N_2} + \frac{\xi_3 x_3}{N_3}\right)\right) \tag{D.2}$$

According to special properties of the Fourier (complex) space, two finite difference schemes are derived for evaluating the Laplacian operator within the SGCP model (Neumann et al., 2002). Further details of this evaluation are provided herein.

$$\mathcal{FFT}\left(\Delta g\right) \simeq \hat{\Delta}\,\mathcal{FFT}\left(g\right) + \begin{cases} \mathrm{O}(dx_i^2) & \text{if the 9-voxel scheme is used} \\ \mathrm{O}(dx_i^4) & \text{if the 21-voxel scheme is used} \end{cases} \tag{D.3}$$

The first and second order partial derivatives based on the 9-voxel finite difference scheme are written for the regular cubic voxel at the position $\left(x_1,x_2,x_3\right)$ in real space as:

$$\frac{\partial g}{\partial x_1} = \frac{g\left(x_1+dx_1,x_2,x_3\right) - g\left(x_1-dx_1,x_2,x_3\right)}{2dx_1} \tag{D.4}$$

[23] For example, in the proposed FFT algorithm, the displacement gradient tensor is a 9-dimensional vector space.

$$\frac{\partial^2 g}{\partial x_1^2} = \frac{g\left(x_1 + dx_1, x_2, x_3\right) - 2g\left(x_1, x_2, x_3\right) + g\left(x_1 - dx_1, x_2, x_3\right)}{dx_1^2} \tag{D.5}$$

Additionally, the derivatives based on the 21-voxel finite difference scheme involve more neighboring voxels in their calculation as:

$$\frac{\partial g}{\partial x_1} = \frac{-g\left(x_1 + 2dx_1, x_2, x_3\right) + 8g\left(x_1 + dx_1, x_2, x_3\right) - 8g\left(x_1 - dx_1, x_2, x_3\right) + g\left(x_1 - 2dx_1, x_2, x_3\right)}{12dx_1} \tag{D.6}$$

$$\frac{\partial^2 g}{\partial x_1^2} = \frac{-g\left(x_1 + 2dx_1, x_2, x_3\right) + 16g\left(x_1 + dx_1, x_2, x_3\right) - 30g\left(x_1, x_2, x_3\right) + 16g\left(x_1 - dx_1, x_2, x_3\right) - g\left(x_1 - 2dx_1, x_2, x_3\right)}{12dx_1^2} \tag{D.7}$$

Consequently, the Laplacian operator associated to these different schemes are derived in Fourier space using the periodicity of Fourier transform and Euler formula.

$$\widehat{\Delta} = \begin{cases} \sum_i \frac{2}{dx_i^2}\left[\cos\left(\xi_i\right) - 1\right] & \text{for 9-voxel scheme} \\ \sum_i \frac{1}{6dx_i^2}\left[-\cos\left(2\xi_i\right) + 16\cos\left(\xi_i\right) - 15\right] & \text{for 21-voxel scheme} \end{cases} \tag{D.8}$$

Appendix E. Time integration

The time integration method solves the constitutive equations to find increments of state variables (Δv^{i+1}) by the implicit *Newton–Raphson* algorithm. In general, the algorithm consists of evaluating residual and Jacobian ($\mathcal{J}^i,\ R^i$) of the respected variables at the previous iteration and updating the state variables, v^{i+1}, until reaching the tolerance.

$$\begin{cases} \mathcal{J}^i(v^i).\Delta v^{i+1} = -R^i(v^i) \\ v^{i+1} = v^i + \Delta v^{i+1} \end{cases} \tag{E.1}$$

The infinitesimal linear elastic strain ($\underset{\sim}{\varepsilon}^{\mathrm{e}}$) and shear strain associated with the slip system (γ^α) are considered for the integration variables and other variables are obtained with respect to these integration variables. Assuming that the variables at the previous time step t_n and the total displacement gradient tensor field at the current time step, $\nabla\underline{u}^{tot}(t_n + \Delta t)$, are known, the residual and their partial derivatives are derived as:

$$R_{\underset{\sim}{\varepsilon}^e} = \Delta\underset{\sim}{\varepsilon}^e + \underset{\sim}{\varepsilon}^e(t_n) - \mathrm{sym}\left(\nabla\underline{u}^{tot}(t_n + \Delta t)\right) + \underset{\sim}{\varepsilon}^p(t_n) + \sum_\alpha \Delta\gamma^\alpha\ \mathrm{sym}(\underline{s}^\alpha \otimes \underline{m}^\alpha) \tag{E.2}$$

$$R_{\gamma^\alpha} = \Delta\gamma^\alpha - \Delta t\ \mathrm{sign}\left(\tau^\alpha\right)\left\langle \frac{\left|\tau^\alpha\right| - \tau_{\mathrm{cr}}^\alpha + S^\alpha}{K}\right\rangle^{\mathrm{n}} \tag{E.3}$$

$$\left(\frac{\partial R_{\underset{\sim}{\varepsilon}^e}}{\partial\Delta\underset{\sim}{\varepsilon}^e}\right)_{ijkl} = \frac{1}{2}\left[\delta_{ik}\delta_{jl} + \delta_{il}\delta_{jk}\right] \tag{E.4}$$

$$\frac{\partial R_{\underset{\sim}{\varepsilon}^e}}{\partial\Delta\gamma^\alpha} = \mathrm{sym}(\underline{s}^\alpha \otimes \underline{m}^\alpha) \tag{E.5}$$

$$\frac{\partial R_{\gamma^\alpha}}{\partial\Delta\underset{\sim}{\varepsilon}^e} = -\Delta t\frac{n}{k}\left\langle \frac{\left|\tau^\alpha\right| - \tau_{\mathrm{cr}}^\alpha + S^\alpha}{K}\right\rangle^{\mathrm{n\text{-}1}} \mathrm{sym}(\underline{s}^\alpha \otimes \underline{m}^\alpha) : \underset{\approx}{C} \tag{E.6}$$

$$\frac{\partial R_{\gamma^\alpha}}{\partial\Delta\gamma^\beta} = \delta_{\alpha\beta}(1 + \Delta t\ \mathrm{sign}\left(\tau^\alpha\ \gamma^\alpha\right)\frac{n}{K}\left\langle \frac{\left|\tau^\alpha\right| - \tau_{\mathrm{cr}}^\alpha + S^\alpha}{K}\right\rangle^{\mathrm{n\text{-}1}}\left[H^\alpha - \frac{\Delta\tau^\alpha\ \exp\left(-\frac{\gamma_{\mathrm{cum}}^\alpha}{\gamma_0}\right)}{\gamma_0}\right]) \tag{E.7}$$

Notably, during the operation of this time integration, it is assumed that the higher order stress from the SGCP model, S, remains constant.

Appendix F. Performance of the FFT-algorithm

To demonstrate superior performance, the proposed FFT-algorithm is compared to the algorithms from previous studies that used the centered scheme Green operator and 9-voxel finite difference scheme. A relatively large single crystal measuring 10 mm × 10 mm is selected and discretized into 64 × 64 voxels. Material parameters are taken from Table 3, using slightly modified $\triangle\tau = 10$ MPa and $\gamma_0 = 0.05$, and $A = 10^{-3}$ N. Tensile loading is applied, as described in Section 3.3, and a defect is positioned at the center to initiate localization. Fig. F.1 presents the results obtained using two different Green operators and finite difference schemes. The localization bands appear ideally smooth when using the rotated Green operator with the 21-voxel scheme. However, with the centered Green operator and the 9-voxel finite difference scheme, the bands exhibit significant oscillations.

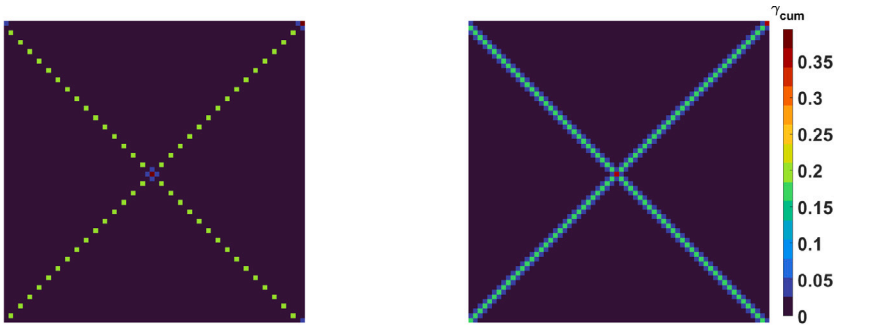

Fig. F.1. The performance of the proposed FFT-algorithm in the SGCP model: a comparison of different Green operators and finite difference schemes in the calculation of the distribution of the cumulative shear strain γ_{cum}.

Data availability

Data will be made available on request.

References

Achouri, M., Germain, G., Dal Santo, P., Saidane, D., 2013. Experimental characterization and numerical modeling of micromechanical damage under different stress states. Mater. Des 50, 207–222.
Ahmadikia, B., Kumar, M.A., Beyerlein, I.J., 2021. Effect of neighboring grain orientation on strain localization in slip bands in hcp materials. Int. J. Plast. 144, 103026.
Ahmadikia, B., Wang, L., Kumar, M.A., Beyerlein, I.J., 2023. Grain boundary slip–twin transmission in titanium. Acta Mater. 244, 118556.
Aifantis, E.C., 1984. On the microstructural origin of certain inelastic models. ASME 106, 326–330.
Aifantis, E.C., 1987. The physics of plastic deformation. Int. J. Plast. 3 (3), 211–247.
Aifantis, E.C., 1992. On the role of gradients in the localization of deformation and fracture. Internat. J. Engrg. Sci. 30 (10), 1279–1299.
Al-Rub, R.K.A., Ettehad, M., Palazotto, A.N., 2015. Microstructural modeling of dual phase steel using a higher-order gradient plasticity–damage model. Int. J. Solids Struct. 58, 178–189.
Arsenlis, A., Parks, D.M., 1999. Crystallographic aspects of geometrically-necessary and statistically-stored dislocation density. Acta Mater. 47 (5), 1597–1611.
Asaro, R., Rice, J., 1977. Strain localization in ductile single crystals. J. Mech. Phys. Solids 25 (5), 309–338.
Berbenni, S., Taupin, V., Djaka, K.S., Fressengeas, C., 2014. A numerical spectral approach for solving elasto-static field dislocation and g-disclination mechanics. Int. J. Solids Struct. 51 (23–24), 4157–4175.
Berbenni, S., Taupin, V., Lebensohn, R.A., 2020. A fast fourier transform-based mesoscale field dislocation mechanics study of grain size effects and reversible plasticity in polycrystals. J. Mech. Phys. Solids 135, 103808.
Boeff, M., Ma, A., Hartmaier, A., 2014. Plastic deformation modelling of tempered martensite steel block structure by a nonlocal crystal plasticity model. Theor. Appl. Mech. Lett. 4 (5), 051007.
Brenner, R., Beaudoin, A.J., Suquet, P., Acharya, A., 2014. Numerical implementation of static field dislocation mechanics theory for periodic media. Phil. Mag. 94 (16), 1764–1787.
Cermelli, P., Gurtin, M.E., 2002. Geometrically necessary dislocations in viscoplastic single crystals and bicrystals undergoing small deformations. Int. J. Solids Struct. 39 (26), 6281–6309.
Chen, Y., Gélébart, L., Marano, A., Marrow, J., 2021. Fft phase-field model combined with cohesive composite voxels for fracture of composite materials with interfaces. Comput. Mech. 68 (2), 433–457.
Clayton, J., 2010. Nonlinear Mechanics of Crystals. Springer Science and Business Media.
Clayton, J.D., McDowell, D.L., Bammann, D.J., 2004. A multiscale gradient theory for single crystalline elastoviscoplasticity. Internat. J. Engrg. Sci. 42 (5–6), 427–457.
Cocke, C.K., Mirmohammad, H., Zecevic, M., Phung, B.R., Lebensohn, R.A., Kingstedt, O.T., Spear, A.D., 2023. A modular spectral solver for crystal plasticity. Int. J. Plast. 162, 103508.
Cordero, N.M., Gaubert, A., Forest, S., Busso, E.P., Gallerneau, F., Kruch, S., 2010. Size effects in generalised continuum crystal plasticity for two-phase laminates. J. Mech. Phys. Solids 58 (11), 1963–1994.
Cui, Y., Po, G., 2018. Suppression of localized plastic flow in irradiated materials. Scr. Mater. 154, 34–39.
Dadhich, R., Alankar, A., 2022. A modular spectral solver for crystal plasticity. Int. J. Plast. 156, 103328.
Di Gioacchino, F., da Fonseca, J.Q., 2015. An experimental study of the polycrystalline plasticity of austenitic stainless steel. Int. J. Plast. 74, 92–109.
Eghtesad, A., Germaschewski, K., Knezevic, M., 2022. Coupling of a multi-gpu accelerated elasto-visco-plastic fast fourier transform constitutive model with the implicit finite element method. Comput. Mater. Sci. 208, 111348.
Eisenlohr, P., Diehl, M., Lebensohn, R.A., Roters, F., 2013. A spectral method solution to crystal elasto-viscoplasticity at finite strains. Int. J. Plast. 46, 37–53.
El Shawish, S., Cizelj, L., 2017. Combining single-and poly-crystalline measurements for identification of crystal plasticity parameters: Application to austenitic stainless steel. Crystals 7 (6), 181.
El Shawish, S., Vincent, P.G., Moulinec, H., Cizelj, L., Gélébart, L., 2020. Full-field polycrystal plasticity simulations of neutron-irradiated austenitic stainless steel: A comparison between fe and fft-based approaches. J. Nucl. Mater. 529, 151927.
Erinosho, T.O., Dunne, F.P.E., 2015. Strain localization and failure in irradiated zircaloy with crystal plasticity. Int. J. Plast. 71, 170–194.
Fleck, N.A., Hutchinson, J.W., 1997. Strain gradient plasticity. Adv. Appl. Mech. 33, 295–361.
Forest, S., 2009. Micromorphic approach for gradient elasticity, viscoplasticity, and damage. J. Eng. Mech. 135 (3), 117–131.

Forest, S., 2016. Nonlinear regularization operators as derived from the micromorphic approach to gradient elasticity, viscoplasticity and damage. Proc. R. Soc. A 472 (2188), 20150755.
Forest, S., Rubin, M.B., 2016. A rate-independent crystal plasticity model with a smooth elastic–plastic transition and no slip indeterminacy. Eur. J. Mech. A Solids 55, 278–288.
Francis, N.M., Pourahmadian, F., Lebensohn, R.A., Dingreville, R., 2024. A fast fourier transform-based solver for elastic micropolar composites. Comput. Methods Appl. Mech. Engrg. 418, 116510.
Gurtin, M.E., 2002. A gradient theory of single-crystal viscoplasticity that accounts for geometrically necessary dislocations. J. Mech. Phys. Solids 50 (1), 5–32.
Gurtin, M.E., 2008. A finite-deformation, gradient theory of single-crystal plasticity with free energy dependent on densities of geometrically necessary dislocations. Int. J. Plast. 24 (4), 702–725.
Hall, E.O., 1951. The deformation and ageing of mild steel: discussion of results. Proc. Phys. Soc. B 64 (9), 747.
Hardie, C., Long, D.J., Demir, E., Tarleton, E., Dunne, F.P., 2023. A robust and efficient hybrid solver for crystal plasticity. Int. J. Plast. 170, 103773.
Hart, E.W., 1967. Theory of the tensile test. Acta Metall. 15 (2), 351–355.
Hesterberg, J., Jiao, Z., Was, G.S., 2019. Effects of post-irradiation annealing on the iascc susceptibility of neutron-irradiated 304l stainless steel. J. Nucl. Mater. 526, 151755.
Howard, C., Bhakhri, V., Dixon, C., Rajakumar, H., Mayhew, C., Judge, C.D., 2019. Coupling multi-scale mechanical testing techniques reveals the existence of a trans-granular channel fracture deformation mechanism in high dose inconel x-750. J. Nucl. Mater. 517, 17–34.
Hure, J., El Shawish, S., Cizelj, L., Tanguy, B., 2016. Intergranular stress distributions in polycrystalline aggregates of irradiated stainless steel. J. Nucl. Mater. 476, 231–242.
Jiao, Z., Was, G.S., 2010. The role of irradiated microstructure in the localized deformation of austenitic stainless steels. J. Nucl. Mater. 407 (1), 34–43.
Joëssel, L., Vincent, P.G., Gărăjeu, M., Idiart, M.I., 2018. Viscoplasticity of voided cubic crystals under hydrostatic loading. Int. J. Solids Struct. 147, 156–165.
Johnson, D.C., Kuhr, B., Farkas, D., Was, G.S., 2019. Quantitative linkage between the stress at dislocation channel–grain boundary interaction sites and irradiation assisted stress corrosion crack initiation. Acta Mater. 170, 166–175.
Kameda, T., Zikry, M.A., 1998. Intergranular and transgranular crack growth at triple junction boundaries in ordered intermetallics. Int. J. Plast. 14 (8), 689–702.
Laghoutaris, P., Chêne, J., Guerre, C., Raquet, O., Sennour, M., Molins, R., Vaillant, F., Scott, P., 2008. Contribution to understanding of stress corrosion cracking of alloy 600 in pwr primary water. Energy Mater. 3 (2), 119–125.
Lame Jouybari, A., El Shawish, S., Cizelj, L., 2023. Crystal plasticity model of austenitic stainless steels subjected to hydrogen concentration and neutron irradiation. In: Proc. Int. Conf. Nucl. Eng.. ICONE, p. 1729.
Lebensohn, R.A., Kanjarla, A.K., Eisenlohr, P., 2012. An elasto-viscoplastic formulation based on fast fourier transforms for the prediction of micromechanical fields in polycrystalline materials. Int. J. Plast. 32, 59–69.
Lebensohn, R.A., Needleman, A., 2016. Numerical implementation of non-local polycrystal plasticity using fast fourier transforms. J. Mech. Phys. Solids 97, 333–351.
Lindroos, M., Scherer, J., Forest, S., Laukkanen, A., Andersson, T., Vaara, J., Mäntylä, A., Frondelius, T., 2022. Micromorphic crystal plasticity approach to damage regularization and size effects in martensitic steels. Int. J. Plast. 151, 103187.
Ling, C., Forest, S., Besson, J., Tanguy, B., Latourte, F., 2018. A reduced micromorphic single crystal plasticity model at finite deformations. application to strain localization and void growth in ductile metals. Int. J. Solids Struct. 134, 43–69.
Lippmann, B.A., Schwinger, J., 1950. Variational principles for scattering processes. Phys. Rev. 79 (3), 469.
Lorentz, E., Benallal, A., 2005. Gradient constitutive relations: numerical aspects and application to gradient damage. Comput. Methods Appl. Mech. Engrg. 194 (50–52), 5191–5220.
Lucarini, S., Segurado, J., 2019. Dbfft: A displacement based fft approach for non-linear homogenization of the mechanical behavior. Internat. J. Engrg. Sci. 144, 103131.
Mahajan, S., Eyre, B.L., 2017. Formation of dislocation channels in neutron irradiated molybdenum. Acta Mater. 122, 259–265.
Marano, A., Gélébart, L., Forest, S., 2019. Intragranular localization induced by softening crystal plasticity: Analysis of slip and kink bands localization modes from high resolution fft-simulations results. Acta Mater. 175, 262–275.
Marano, A., Gélébart, L., Forest, S., 2021. Fft-based simulations of slip and kink bands formation in 3d polycrystals: Influence of strain gradient crystal plasticity. J. Mech. Phys. Solids 149, 104295.
Matlab, R., 2022. Release, s. t. 2022a. The MathWorks, Inc., Natick, Massachusetts, United States.
McMurtrey, M., Was, G., Patrick, L., Farkas, D., 2011. Relationship between localized strain and irradiation assisted stress corrosion cracking in an austenitic alloy. Mater. Sci. Eng. 528, 3730–3740.
Michel, J.C., Moulinec, H., Suquet, P., 1999. Effective properties of composite materials with periodic microstructure: a computational approach. Comput. Methods Appl. Mech. Engrg. 172 (1–4), 109–143.
Miehe, C., Schröder, J., 2001. A comparative study of stress update algorithms for rate-independent and rate-dependent crystal plasticity. Internat. J. Numer. Methods Engrg. 50 (2), 273–298.
Moulinec, H., Suquet, P., 1998. A numerical method for computing the overall response of nonlinear composites with complex microstructure. Comput. Methods Appl. Mech. Engrg. 157 (1–2), 69–94.
Needleman, A., 1988. Material rate dependence and mesh sensitivity in localization problems. Comput. Methods Appl. Mech. Engrg. 67 (1), 69–85.
Nellemann, C., Niordson, C.F., Nielsen, K.L., 2017. An incremental flow theory for crystal plasticity incorporating strain gradient effects. Int. J. Solids Struct. 110, 239–250.
Neumann, S., Herrmann, K.P., Müller, W.H., 2002. Stress/strain computation in heterogeneous bodies with discrete fourier transforms—-different approaches. Comput. Mater. Sci. 25 (1–2), 151–158.
Nguyen, T.K., 2010. Homogénéisation Numérique de Structures Périodiques par Transformée de Fourier: Matériaux Composites et Milieux Poreux (Doctoral dissertation). Université Paris-Est.
Niordson, C.F., Kysar, J.W., 2014. Computational strain gradient crystal plasticity. J. Mech. Phys. Solids 62, 31–47.
Nye, J.F., 1953. Some geometrical relations in dislocated crystals. Acta Metall. 1 (2), 153–162.
Onimus, F., Béchade, J.L., 2009. A polycrystalline modeling of the mechanical behavior of neutron irradiated zirconium alloys. J. Nucl. Mater. 384 (2), 163–174.
Onimus, F., Béchade, J.L., Duguay, C., Gilbon, D., Pilvin, P., 2006. Investigation of neutron radiation effects on the mechanical behavior of recrystallized zirconium alloys. J. Nucl. Mater. 358 (2–3), 176–189.
Peerlings, R.H.J., Poh, L.H., Geers, M.G.D., 2012. An implicit gradient plasticity–damage theory for predicting size effects in hardening and softening. Eng. Fract. Mech. 95, 2–12.
Petch, N.J., 1953. The cleavage strength of polycrystals. Iron Steel Inst. 174, 25–28.
Pokor, C., Brechet, Y., Dubuisson, P., Massoud, J.P., Averty, X., 2004. Irradiation damage in 304 and 316 stainless steels: experimental investigation and modeling. part ii: Irradiation induced hardening. J. Nucl. Mater. 326 (1), 30–37.
Quey, R., Dawson, P.R., Barbe, F., 2011. Large-scale 3d random polycrystals for the finite element method: Generation, meshing and remeshing. Comput. Methods Appl. Mech. Engrg. 200 (17–20), 1729–1745.
Ramière, I., Helfer, T., 2015. Iterative residual-based vector methods to accelerate fixed point iterations. Comput. Math. Appl. 70 (9), 2210–2226.

Rezvanian, O., Zikry, M.A., Rajendran, A.M., 2007. Statistically stored, geometrically necessary and grain boundary dislocation densities: microstructural representation and modelling. Proc. R. Soc. A 463 (2087), 2833–2853.
Rice, J., 1976. The localization of plastic deformation. In: Koiter, W.T. (Ed.), Theoretical and Applied Mechanics (Proceedings of the 14th International Congress on Theoretical and Applied Mechanics). North-Holland Publishing CO., pp. 207–220.
Rogers, H.C., 1979. Adiabatic plastic deformation. Annu. Rev. Mater. Sci. 9 (1), 283–311.
Scherer, J.M., Besson, J., Forest, S., Hure, J., Tanguy, B., 2019. Strain gradient crystal plasticity with evolving length scale: Application to voided irradiated materials. Eur. J. Mech. A Solids 77, 103768.
Scherer, J.M., Phalke, V., Besson, J., Forest, S., Hure, J., Tanguy, B., 2020. Lagrange multiplier based vs micromorphic gradient-enhanced rate-(in) dependent crystal plasticity modelling and simulation. Comput. Methods Appl. Mech. Engrg. 372, 113426.
Simulia, 2015. Abaqus 6.13-4. Dassault Systèmes Simulia Corporation; Dassault Systèmes, Providence, RI, USA.
Tang, X., Wang, Z., Wang, X., Deng, L., Zhang, M., Gong, P., Jin, J., Fu, M.W., 2023. Unraveling size-affected plastic heterogeneity and asymmetry during micro-scaled deformation of cp-ti by non-local crystal plasticity modeling. Int. J. Plast. 170, 103733.
Thomas, R., Lunt, D., Atkinson, M., da Fonseca, J., Preuss, M., Barton, F., O'Hanlon, J., Frankel, P., 2019. Characterisation of irradiation enhanced strain localisation in a zirconium alloy. Materialia 5, 100248.
Waffenschmidt, T., Polindara, C., Menzel, A., Blanco, S., 2014. A gradient-enhanced large-deformation continuum damage model for fibre-reinforced materials. Comput. Methods Appl. Mech. Engrg. 268, 801–842.
Willot, F., 2015. Fourier-based schemes for computing the mechanical response of composites with accurate local fields. C. R. Méc. 343 (3), 232–245.
Wulfinghoff, S., Bayerschen, E., Böhlke, T., 2013. A gradient plasticity grain boundary yield theory. Int. J. Plast. 51, 33–46.
Wulfinghoff, S., Böhlke, T., 2012. Equivalent plastic strain gradient enhancement of single crystal plasticity: theory and numerics. Proc. R. Soc. A 468 (2145), 2682–2703.
Xue, Z., Pontin, M.G., Zok, F.W., Hutchinson, J.W., 2010. Calibration procedures for a computational model of ductile fracture. Eng. Fract. Mech. 77 (3), 492–509.
You, X., Yang, J., Dan, C., Shi, Q., Zhong, S., Wang, H., Chen, Z., 2023. Statistical analysis of slip transfer in al alloy based on in-situ tensile test and high-throughput computing method. Int. J. Plast. 166, 103649.
Zecevic, M., Lebensohn, R.A., Capolungo, L., 2022. New large-strain fft-based formulation and its application to model strain localization in nano-metallic laminates and other strongly anisotropic crystalline materials. Mech. Mater. 166, 104208.
Zecevic, M., Lebensohn, R.A., Capolungo, L., 2023. Non-local large-strain fft-based formulation and its application to interface-dominated plasticity of nano-metallic laminates. J. Mech. Phys. Solids 173, 105187.
Zener, C., Hollomon, J.H., 1944. Effect of strain rate upon plastic flow of steel. J. Appl. Phys. 15 (1), 22–32.
Zhang, R., Xu, Z., Peng, L., Lai, X., Fu, M.W., 2022. Intragranularly misoriented grain boundary evolution affected by local constraints and grain size in micro-scale deformation of ultra-thin metallic sheets. Int. J. Plast. 157, 103377.
Zhang, X., Zhao, J., Kang, G., Zaiser, M., 2023. Geometrically necessary dislocations and related kinematic hardening in gradient grained materials: A nonlocal crystal plasticity study. Int. J. Plast. 163, 103553.